Design of High Efficiency Mid IR QCL Lasers

by

Allen Long Hsu

B.S., Electrical Engineering
Princeton University (2006)

Submitted to the Department of Electrical Engineering and Computer Science
in partial fulfillment of the requirements for the degree of

Masters of Science in Computer Science and Engineering

at the

MASSACHUSETTS INSTITUTE OF TECHNOLOGY

September 2008

Author .....
Department of Electrical Engineering and Computer Science
August 29, 2008

Certified by .....
Qing Hu
Professor of Electrical Engineering
Thesis Supervisor

Accepted by .....
Terry P. Orlando
Chairman, Department Committee on Graduate Theses

Design of High Efficiency Mid IR QCL Lasers

by

Allen Long Hsu

Submitted to the Department of Electrical Engineering and Computer Science
on August 29, 2008, in partial fulfillment of the
requirements for the degree of
Masters of Science in Computer Science and Engineering

Abstract

The proposed research is a study of designing high-efficiency Mid-IR quantum cascade lasers (QCL). This thesis explores "injector-less" designs for achieving lower voltage defects and improving wall plug efficiences through highly strain-balanced structures and minimized injector regions. This work contains experimental design work for testing and evaluating Mid-IR QCL performance, simulation work for verifying wavefunction and energy alignment, as well as, Monte Carlo transport simulations for evaluating designs, and finally measuring lasing and spontaneous emission performance for various designs.

Thesis Supervisor: Qing Hu
Title: Professor of Electrical Engineering

Acknowledgments

I want to acknowledge the help from my advisor and the other grad students in the Hu Lab for their help and guidance in this project. Furthermore, I want to thank MIT Lincoln Lab for their assistance with growing and fabricating devices for the project. Finally, I want to thank family and friends for their support during this entire process.

Contents

List of Figures

List of Tables

Chapter 1

Introduction

Quantum Cascade Lasers (QCL) since their invention in 1994 have become the dominant source for compact, robust, tunable, high powered lasers in the mid-infrared (Mid-IR) spanning 3 to 20 μm [4]. Current QCL performance ranges from 300-400K and CW power of 1.6 W [5]. The main driving factors behind these squrces are numerous sensing applications in the Mid-IR. Chemical spectroscopy and trace gas sensing are the most common areas due to strong spectroscopic signatures in the Mid-IR caused by molecular vibrational resonances. Furthermore, due to low atmospheric absorption between 3 to 5 μm work is being done on developing communication links that would be stable irrespective of weather conditions as well as infrared counter measures. These applications for a portable Mid-IR laser source motivate the need for an efficient lasing source, in order to reduce the need for excessive cooling and power supplies. Currently, the maximum wall plug efficiency (WPE) is only 12 % WPE under CW conditions [5]; however the desired WPE for these applications would ideally be 25-50 %. Therefore, there is still a lot of work necessary to achieve these performance levels. The quantum cascade laser is a powerful example of band structure engineering. The original concept for a QCL dated back to 1971 by Kazarinov and Suris [6]. However, it was not until 1994 that the concept was first demonstrated. With the development of heterostructure quantum wells, electronic states could be engineered into a laser structure. Unlike traditional interband semiconductor lasers which rely on the intrinsic properties of the materials to define the wavelength, QCL's emission wavelength can be engineered by varying the thickness of the quantum wells. This flexibility means with a given material system such as InGaAs/InAlAs various wavelength lasers can be made. Designing these quantum wells has yielded many various configurations and design paradigms, one of which the

"injectorless" will be the primary focus of this work.[1].

A Quantum Cascade Laser (QCL) is a series of quantum wells grown in a periodic manner that create a cascaded structure of energy states when a voltage bias is applied. Semiconductors when grown on top of different semiconductors form heterojunction quantum wells. These quantum wells provide confinement for electrons. The appropriate energy levels and confined states can solved by using Effective Mass theory to simplify the problem down to a 1-D Schroedinger equation. Solving for the quantized states in these heterostructures is similar to solving "particle in a box"-like problems as shown in the energy band diagram in figure 1-1. Electrons sit in these

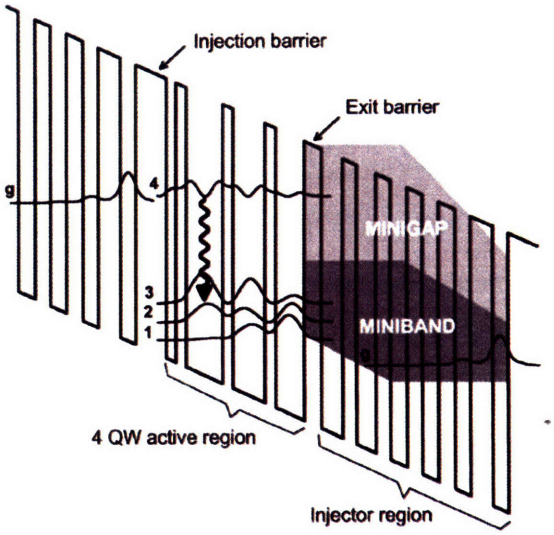

Figure 1-1: Two Phonon Design with miniband injector [1]

energy states and with an applied electric field, cause current to pass through these devices. In figure 1-1, an electric field has been applied to bring levels (g) and (4) into alignment. Electrons in (g) tunnel into level (4); the rate of tunneling is controlled by the thickness of the injection barrier. Electrons in level (4) due to a strong coupling with light fall to level (3) and emit a photon. Electrons in level (3) can also absorb a photon and become excited into level (4). Therefore, for proper lasing to occur, we require a population inversion between levels (3) and (4). To achieve this, electrons in level (3) need to scatter quickly to lower levels (2) and (1). By designing the level pairs (3),(2) and (2),(1) to each be resonant with a Polar Longitudinal Phonon or lattice vibration, electrons in level (3) can rapidly scatter into lower states. Level (1) was introduced to prevent thermally excited electrons in (2) from backscattering into (3). Electrons then transit

from one module to the next through a quasi-continuum of states or miniband. This process is repeated for each module, typically 30-40 modules; electrons are recycled allowing one electron to emit one photon per module. The two-phonon design with miniband presented here has so far produced some of the highest wall plug efficiencies and CW performance.

It was originally thought that a miniband was necessary for proper device operation and stable current injection. However, recently a series of papers have explored the possibility of an "injectorless" design [7] [8] [2]. Essentially, these designs remove the miniband and electrons from the active region are directly injected into the next. These injectorless designs have already

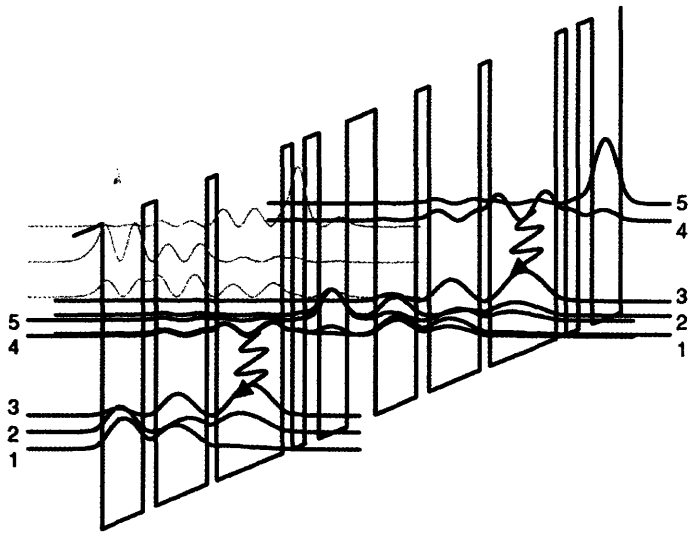

Figure 1-2: Injectorless Design [2]

demonstrated room temperature CW performance and some of the lowest threshold operation $\approx$ 0.150 kA/cm^2 [2] at 77K; however, the performance drops at 300K. Furthermore, these injectorless designs have some promising benefits for higher WPE that have not yet been fully explored. This will be covered in chapter 2, when deriving the metrics responsible for WPE.

Therefore, the work presented here will focus on the injectorless design as an approach for higher WPE. This includes:

1. **Theory** - Fundamentals of effective mass theorem, nonparabolicity, spontaneous and stimulated emission, nonradiative scattering, resonant tunneling, and WPE.

2. **Simulation** - Band Structure and Monte Carlo Simulations of QCL

3. **Experimental Setup** - Design and construction of device characterization Software and Hardware

4. **Designs** - New Designs for Injectorless Structure

5. **Measurements** - Preliminary measurements of samples as well and Fourier Transform Hakki-Paoli Method for measuring waveguide loss.

Chapter 2

Theory

The theory behind quantum cascade lasers involves understanding the underlying electron transport and scattering in semiconductors, as well as, how light and matter interact. Therefore, we will focus initially on describing electrons in solids and heterostructures through envelope formalism. This formalism simplifies the microscopic details of a system and allows electrons to be described by a simple envelope function. These envelope functions will be important later on for computing electron scattering as well as spontaneous and stimulated emission.

2.1 $\vec{\mathbf{k}} \cdot \vec{\mathbf{p}}$ Hamiltonian

In order to describe an electron in a solid, we must first derive the bandstructure in a semiconductor. This derivation for the K.P. Hamiltonian follows from references [9] [10]. For a semiconductor we can write down the time-independent Hamiltonian for the system.

$$\left[\frac{p^2}{2m_0} + V(\mathbf{r}) + \frac{\hbar}{4m_0^2c^2}(\sigma \times \nabla V) \cdot \mathbf{p}\right]\psi(\mathbf{r}) = E\psi(\mathbf{r}) \tag{2.1}$$

$$V\left(\mathbf{r} + \sum_i n_i \mathbf{a_i}\right) = V(\mathbf{r}) \tag{2.2}$$

In equation (2.1), the third term describes the spin-orbit coupling term. Because we have assumed a periodic potential, the solution $\psi(\mathbf{r})$ to (2.1) takes the form of a Bloch wavefunction (2.3).

$$\psi_{n\mathbf{k}}(\mathbf{r}) = N u_{n\mathbf{k}}(\mathbf{r}) e^{i\mathbf{k}\cdot\mathbf{r}} \tag{2.3}$$

where N is a normalization coefficient. The Bloch wavefunction is labeled by n and k, the electronic band and crystal momentum respectively. Assuming this bloch form for the wavefunction we can obtain equation (2.4) by substituting (2.3) into (2.1)

$$E_{n\mathbf{k}}u_{n\mathbf{k}} = \left[\frac{p^2}{2m_0} + V(\mathbf{r}) + \frac{\hbar}{4m_0^2c^2}(\sigma \times \nabla V)\cdot\mathbf{p} + \frac{\hbar^2k^2}{2m_0} + \frac{\hbar\mathbf{k}}{m_0}\cdot\left(\mathbf{p} + \frac{\hbar}{4m_0c^2}\sigma\times\nabla V\right)\right]u_{n\mathbf{k}} \quad (2.4)$$

As is often the case, we are concerned about describing electrons at high symmetry points such as the Γ or $\mathbf{k} = 0$. In order to solve (2.4) we can take a perturbative approach by expressing the solutions in terms of known solutions at $\mathbf{k} = 0$.

Assume the unperturbed hamiltonian for $\mathbf{k} = 0$ does not include effects due to spin orbit coupling.

$$H_0 = \frac{p^2}{2m_0} + V(\mathbf{r}) \quad (2.5)$$

$$H_0u_{n\mathbf{0}} = E_{n\mathbf{0}}u_{n\mathbf{0}} \quad (2.6)$$

Therefore $u_{n\mathbf{0}}$, assuming a tight binding method, represents S and P atomic orbitals centered on the periodic lattice sites. Adding back the spin-orbit coupling terms as a perturbation allows us to use a finite basis expansion to expand the solution in terms of these atomic orbital terms.

$$H = H_0 + \frac{\hbar}{m_0}\mathbf{k}\cdot\mathbf{p} + \frac{\hbar^2}{4m_0^2c^2}(\nabla V\times\mathbf{k})\cdot\sigma + \frac{\hbar^2}{4m_0^2c^2}(\nabla V\times\mathbf{p})\cdot\sigma \quad (2.7)$$

$$E'_{n\mathbf{k}} = E_{n\mathbf{k}} - \frac{\hbar^2k^2}{2m_0} \quad (2.8)$$

In most cases, $|\mathbf{k}| \ll |\mathbf{p}|$, so we drop the third term in H.

$$H \approx H_0 + \frac{\hbar}{m_0}\mathbf{k}\cdot\mathbf{p} + \frac{\hbar^2}{4m_0^2c^2}(\nabla V\times\mathbf{p})\cdot\sigma \quad (2.9)$$

Using the complete basis centered at Γ we can write our full solution as a sum of the $\mathbf{k} = \mathbf{0}$ states.

$$u_{n\mathbf{k}}(\mathbf{r}) = \sum_l a_l(\mathbf{k})u_{l\mathbf{0}}(\mathbf{r}) \quad (2.10)$$

where l is the electronic bands at $\mathbf{k} = 0$ and $a_l(\mathbf{k})$ represents the weighting coefficients for the various basis states.

Table 2.1: Basis Functions $u_{n0}(\mathbf{r})$

n	$\lvert J, m_j\rangle$	$u_{n0}(\mathbf{r})$	E_{n0}
$u_{10}(\mathbf{r})$	$\lvert\frac{1}{2}, \frac{1}{2}\rangle$	$i\lvert S, \uparrow\rangle$	0
$u_{20}(\mathbf{r})$	$\lvert\frac{3}{2}, \frac{1}{2}\rangle$	$-\sqrt{\frac{2}{3}}\lvert P_z, \uparrow\rangle + \sqrt{\frac{1}{6}}\lvert P_x + iP_y, \downarrow\rangle$	$-E_g$
$u_{30}(\mathbf{r})$	$\lvert\frac{3}{2}, \frac{3}{2}\rangle$	$\sqrt{\frac{1}{2}}\lvert P_x + iP_y, \uparrow\rangle$	$-E_g$
$u_{40}(\mathbf{r})$	$\lvert\frac{1}{2}, \frac{1}{2}\rangle$	$\sqrt{\frac{1}{3}}\lvert P_z, \uparrow\rangle + \sqrt{\frac{1}{3}}\lvert P_x + iP_y, \downarrow\rangle$	$-E_g - \Delta$
$u_{50}(\mathbf{r})$	$\lvert\frac{1}{2}, -\frac{1}{2}\rangle$	$i\lvert S, \downarrow\rangle$	0
$u_{60}(\mathbf{r})$	$\lvert\frac{3}{2}, -\frac{1}{2}\rangle$	$-\sqrt{\frac{2}{3}}\lvert P_z, \downarrow\rangle - \sqrt{\frac{1}{6}}\lvert P_x - iP_y, \uparrow\rangle$	$-E_g$
$u_{70}(\mathbf{r})$	$\lvert\frac{3}{2}, -\frac{3}{2}\rangle$	$\sqrt{\frac{1}{2}}\lvert P_x - iP_y, \downarrow\rangle$	$-E_g$
$u_{80}(\mathbf{r})$	$\lvert\frac{1}{2}, -\frac{1}{2}\rangle$	$\sqrt{\frac{1}{3}}\lvert P_z, \downarrow\rangle - \sqrt{\frac{1}{3}}\lvert P_x - iP_y, \uparrow\rangle$	$-E_g - \Delta$

Where in Table 2.1, we have defined the following terms.

$$E_g := E_s - E_p - \frac{1}{3}\Delta \tag{2.11}$$

$$\Delta = 3i\langle P_y|\frac{\hbar}{4m_0^2c^2}\left(\frac{\partial V}{\partial x}p_y - \frac{\partial V}{\partial y}p_x\right)|P_x\rangle \tag{2.12}$$

Given our full Hamiltonian including perturbation and applying a finite basis expansion, we can solve for the weighting coefficients.

$$\sum_{m=1}^{8}\left[\langle u_{n0}(\mathbf{r})|H|u_{m0}(\mathbf{r})\rangle - E'_{n\mathbf{k}}\right]a_n(\mathbf{k}) = 0 \tag{2.13}$$

$$H_{nm} = \langle u_{n0}(\mathbf{r})|H|u_{m0}(\mathbf{r})\rangle = \begin{pmatrix} H_1 & H_2 \\ H_2^* & H_1 \end{pmatrix}$$

Where the Kane parameter is $P = -i\frac{\hbar}{m_0}\langle S|p_i|P_i\rangle \in (x, y, z)$ and $k_\pm = \frac{1}{\sqrt{2}}(k_x \pm ik_y)$. These matrix elements can be computed by applying symmetry and parity properties of the Bloch

Table 2.2: $H_1 = \langle u_{n0}(\mathbf{r})|H|u_{m0}(\mathbf{r})\rangle$

	u_{10}	u_{20}	u_{30}	u_{40}
u_{10}	0	$-\sqrt{\frac{2}{3}}Pk_z$	Pk_+	$\sqrt{\frac{1}{3}}Pk_z$
u_{20}	$-\sqrt{\frac{2}{3}}Pk_z$	$-E_g$	0	0
u_{30}	Pk_-	0	$-E_g$	0
u_{40}	$\sqrt{\frac{1}{3}}Pk_z$	0	0	$-E_g-\Delta$

Table 2.3: $H_2 = \langle u_{n0}(\mathbf{r})|H|u_{m0}(\mathbf{r})\rangle$

	u_{50}	u_{60}	u_{70}	u_{80}
u_{10}	0	$-\sqrt{\frac{1}{3}}Pk_-$	0	$-\sqrt{\frac{2}{3}}Pk_-$
u_{20}	$\sqrt{\frac{1}{3}}Pk_-$	0	0	0
u_{30}	0	0	0	0
u_{40}	$\sqrt{\frac{2}{3}}Pk_-$	0	0	0

atomic orbitals [10].

Fully solving the 8x8 K.P. Hamiltonian in equation (2.13) will yield the energy dispersion (E vs. k) relationship for the conduction, light, heavy hole, and split off bands. This provides a method for estimating the band structure of a material by utilizing known solutions around a fixed **k** point. Furthermore the microscopic properties of the material have been absorbed into the Kane Parameter and Spin Orbit Split Off, which can be estimated experimentally.

Because we are dealing with bulk materials, we can choose to an orientation where **k**//J//z. This choice of direction, greatly simplifies the math due to the decoupling of many of the basis states from each other. Table 2.4 shows the reduced k.p matrix.

The characteristic equation for the eigenvalues of this matrix are $E'_{n\mathbf{k}} = -E_g$ or

$$(E'_{n\mathbf{k}})(E'_{n\mathbf{k}} + E_g)(E'_{n\mathbf{k}} + E_g + \Delta) = k^2P^2(E'_{n\mathbf{k}} + E_g + \frac{2\Delta}{3}) \tag{2.14}$$

while no closed form expression exists for the eigenvalues, we can solve for the conduction band energy dispersion by assuming that $|\mathbf{k}|$ is located near the Γ pt, so we can look at the lower

Table 2.4: $H_1 = \langle u_{n0}(\mathbf{r})|H|u_{m0}(\mathbf{r})\rangle$

	u_{10}	u_{20}	u_{30}	u_{40}
u_{10}	0	$-\sqrt{\frac{2}{3}}Pk_z$	0	$\sqrt{\frac{1}{3}}Pk_z$
u_{20}	$-\sqrt{\frac{2}{3}}Pk_z$	$-E_g$	0	0
u_{30}	0	0	$-E_g$	0
u_{40}	$\sqrt{\frac{1}{3}}Pk_z$	0	0	$-E_g-\Delta$

order terms of $E_c = 0 + \epsilon(k^2)$.

$$E_{\mathbf{ck}} = E_c(\mathbf{k}) = \frac{\hbar^2 k^2}{2}\left[\frac{1}{m_0} + \frac{4P^2}{3\hbar^2 E_g} + \frac{2P^2}{3\hbar^2(E_g+\Delta)}\right] = \frac{\hbar^2 k^2}{2m_c^*} \tag{2.15}$$

Looking at the 4 possible solution, near the band edge, we see that the heavy hole states decouple and are not dependent on k. In order to include the curvature of the heavy hole, one needs to consider inclusion of remote band effects, which are derived by Bastard [9]. Even though the k.p. hamiltonian solves for the bulk bandstructure of semiconductor, we will show shortly its use for describing electrons in heterostructure quantum wells.

2.2 Envelope Approximation

For devices of interest, we are concerned with describing electronic waveforms of semiconductor heterostructures. Heterostructures are made from growing layers of different materials on top of one another. Due to differences in band alignments between materials, quantum wells and thus electronic confinement are created. By assuming that the scale of variation of the materials is greater than the actual atomic variation, an envelope approximation can be used to greatly simplify the problem. This envelope approximation is otherwise known as the Effective Mass Theorem [9] [10]. Therefore, the solution for the various bound states and energy values can be reduced to solving equation (2.16), where $\mathbf{k} \rightarrow i\nabla$.

$$\left[\sum_m H_{nm}(k = -\mathbf{i}\nabla)F_m(\mathbf{r}) + F_n(\mathbf{r})U(\mathbf{r})\right] = EF_n(\mathbf{r}) \tag{2.16}$$

Where $F_n(\mathbf{r})$ represents the envelope function for band (n), and U($\mathbf{r}$) is the slowly varying potential. For most cases, our perturbation is due to the various band offsets in the growth direction. Therefore, let us limit U($\mathbf{r}$) to U(z). While solving equation (2.16) yields an accurate solution, this equation can be written in its more common form for the conduction band, by utilizing equation (2.13)

$$[E_n(\mathbf{k} = -\mathbf{i}\nabla) + U(z)]F_n(\mathbf{r}) = EF_n(\mathbf{r}) \tag{2.17}$$

Using equation (2.15), we can rewrite equation (2.17).

$$\frac{-\hbar^2\nabla_\perp^2}{2m_c^*(z)}F_c(\mathbf{r}) + \frac{-\hbar^2}{2}\nabla_z\frac{1}{m_c^*(z)}\nabla_z F_c(\mathbf{r}) + U(z)F_c(\mathbf{r}) = EF_c(\mathbf{r}) \tag{2.18}$$

From equation (2.18) the envelope wavefunction takes on the form

$$F_c(\mathbf{r}) = \frac{1}{\sqrt{S}}e^{i\mathbf{k}_\perp\cdot\mathbf{r}_\perp}F_c(z) \tag{2.19}$$

Substituting equation (2.19) into (2.18), we get

$$\frac{-\hbar^2 k_\perp^2}{2m_c^*(z)}F_c(z) + \frac{-\hbar^2}{2}\nabla_z\frac{1}{m_c^*(z)}\nabla_z F_c(z) + U(z)F_c(z) = EF_c(z) \tag{2.20}$$

Equation (2.20) couples $k_\perp$ with z, which complicates the problem. For simplicity, we assume parabolic subbands in $k_\perp$ with the effective mass of the well.

$$\frac{-\hbar^2}{2}\nabla_z\frac{1}{m_c^*(z)}\nabla_z F_c(z) + U(z)F_c(z) = \left(E + \frac{\hbar^2 k_\perp^2}{2m_c^*}\right)F_c(z) \tag{2.21}$$

Equation (2.21) takes on the simplified form of a 1-D Schroedinger Equation, where the microscopic properties of the material are grouped into the effective mass parameter. This equation assumes parabolic bands close to the band minimum; however, for most Mid-IR device, this is not the case. Therefore, we must introduce higher order effects to deal with non-parabolic bands . A common approach involves using an energy dependent effective mass, which can be derived explicitly by solving the full k.p. Hamiltonian in equation (2.16).

To reduce the complexity of the problem, we still assume parabolic subbands in $k_\perp$, but we

ignore the free electron terms $\frac{\hbar^2 k^2}{2m_0}$, which contribute terms on the order of $(E_c - E_{lh,so})/E_p \ll 1$. Therefore if we assume $k \in (0, 0, k_z)$ we arrive at the set of equations

$$\begin{pmatrix} E_c(z) & \sqrt{\frac{2}{3}}Pk_z & -\sqrt{\frac{1}{3}}Pk_z \\ \sqrt{\frac{2}{3}}Pk_z & E_{lh}(z) & 0 \\ -\sqrt{\frac{1}{3}}Pk_z & 0 & E_{so}(z) \end{pmatrix} \begin{pmatrix} F_c(z) \\ F_{lh}(z) \\ F_{so}(z) \end{pmatrix} = E \begin{pmatrix} F_c(z) \\ F_{lh}(z) \\ F_{so}(z) \end{pmatrix}$$

Implicitly, the Bloch components of the different materials are taken to be equal. This is because the Kane Parameter (P) does not change significantly between the well and the barrier material. The only change between the well and the barrier is due to different energy alignments of the conduction, light-hole and split off bands. We can write the closed form solution by explicitly cross eliminating the light hole and split off envelope functions from the first row of k.p. matrix, which yields

$$p_z \frac{1}{2m(E,z)} p_z F_c + E_c(z) F_c = E F_c \tag{2.22}$$

$$m(E,z) = m_0 \frac{E - E_v(z)}{E_p} \tag{2.23}$$

Where $E_v(z) = (2E_{lh}(z) + E_{so}(z))/3$ is the effective valence band and $P = i\frac{E_p}{2m_0}$ [11]. We can rewrite equation (2.23) in terms of conduction band effective mass in a material $m_c^* = m_0(E_c - E_v)/E_p$.

$$m(E,z) = m_c^*(z)\left(1 + \frac{E - E_c(z)}{E_c(z) - E_v(z)}\right)$$

As for the appropriate boundary conditions, we assume the continuity of

1. F_c

2. $\frac{1}{m_c^*(E,z)} \frac{dF_c}{dz}$

Figure (2-1) shows the importance of nonparabolicity away from the conduction band edge for the upper lasing level.

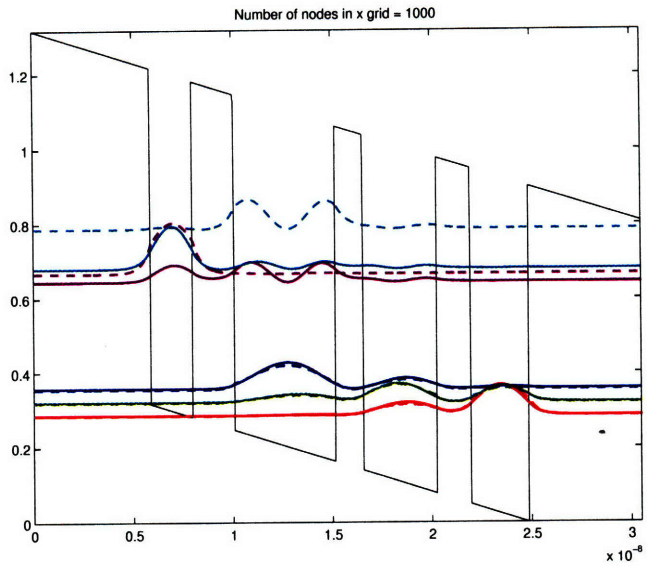

Figure 2-1: Effect of Nonparabolicity on QCL energy levels. Dotted lines are without nonparabolicity, solid lines are with nonparabolicity

2.3 Intersubband radiative transitions and gain

Given the envelope wavefunction for an electron in a quantum well, we can now describe optical processes for lasers such as spontaneous and stimulated emission. We first need to derive the interaction hamiltonian due to light. From the Lorentz Force Law, we know

$$F = q(\mathbf{E} + \mathbf{v} \times \mathbf{B}) \tag{2.24}$$

$$\mathbf{E} = -\nabla\phi - \frac{\partial \mathbf{A}}{\partial \mathbf{t}} \tag{2.25}$$

$$\mathbf{B} = \nabla \times \mathbf{A} \tag{2.26}$$

Where, $\mathbf{B}$ and $\mathbf{E}$ are the magnetic and electric fields, and $\mathbf{A}$ and ϕ are the magnetic vector potential and electric scalar potential. The Lagrangian is defined

$$L = KE - U \tag{2.27}$$

Where KE is the kinetic energy, and U is the potential energy. Therefore, under this definition we can also define the force in terms of U.

$$F_x = -\frac{\partial U}{\partial x} + \frac{d}{dt}\left(\frac{\partial U}{\partial \dot{x}}\right) \tag{2.28}$$

The solution to this equation in terms of the scalar and vector potentials is

$$U = q(\phi - \mathbf{v} \cdot \mathbf{A}) \tag{2.29}$$

Therefore, classically we can write out explicitly the Lagrangian in terms of position and velocity.

$$L(r, v) = \frac{1}{2}mv^2 - q(\phi - \mathbf{v} \cdot \mathbf{A}) \tag{2.30}$$

Furthermore, we can express velocity in terms of canonical momentum.

$$p_x = \frac{\partial L(r, v)}{\partial v_x} = mv_x + qA_x \tag{2.31}$$

$$\mathbf{v} = \frac{1}{m}(\mathbf{p} - q\mathbf{A}) \tag{2.32}$$

Upon substitution of equation (2.32) into (2.30), we can define a constant of motion

$$E = q\phi + \frac{1}{2m}(\mathbf{p} - q\mathbf{A})^2 \tag{2.33}$$

Since we are considering the interaction of light and electron in a solid, we will assume the mass is the effective mass (m^*). We can also write the quantum mechanical hamiltonian by replacing variables with their analogous quantum mechanical operators. If we assume a Coulomb Gauge $\nabla \cdot \mathbf{A} = \mathbf{0}$, the interaction hamiltonian is

$$H_{int} = -\frac{q}{m^*}\mathbf{A} \cdot \mathbf{p} \tag{2.34}$$

Where $\mathbf{A}$ and $\mathbf{p}$ are operators now. To compute optical transitions we apply the results of time-dependent perturbation theory and Fermi's Golden Rule.

$$W_{i \to f} = \frac{2\pi}{\hbar}|\langle i|H_{int}|f\rangle|^2 \delta(E_f - E_i \pm \hbar\omega) \tag{2.35}$$

Where in equation (2.35) the time oscillations of the field have already been accounted for in the interaction hamiltonian and are represented in the delta function. (i) and (f) represent the full initial and final wavefunction states of the system. This explicitly includes the envelope functions, Bloch functions of the electrons, as well as the photon field. The description of the photon fields is the result of second quantization, which is derived in [12].

$$|i\rangle = |\mathbf{k}_i\rangle|n_{\mathbf{q},\sigma}\rangle \tag{2.36}$$

$$|f\rangle = |\mathbf{k}_f\rangle|m_{\mathbf{q},\sigma}\rangle \tag{2.37}$$

$$|\mathbf{k}_i\rangle = u_{v_i}(\mathbf{r})\frac{1}{\sqrt{S}}\exp(i\mathbf{k}_\perp \cdot r_\perp)F_i(z) \tag{2.38}$$

n and m represent the photon number in the cavity with polarization σ and in mode $\mathbf{q}$, and $u_{v_i}(r)$ represents the initial bloch wavefunction for band (v), and S is the normalization factor. Utilizing the results from second quantization of the field we can express $\mathbf{A}$ in terms of lowering and raising operators that act only on the photon number.

$$\mathbf{A} = \sqrt{\frac{\hbar}{2\epsilon\omega_\mathbf{q}V}}\hat{e}_{\mathbf{q},\sigma}\left[a_{\mathbf{q},\sigma}e^{i\mathbf{q}\cdot\mathbf{r}} + a^\dagger_{\mathbf{q},\sigma}e^{-i\mathbf{q}\cdot\mathbf{r}}\right] \tag{2.39}$$

Substituting equation (2.39) into the matrix element of Fermi's Golden Rule, we get

$$\langle i|H_{int}|f\rangle = -\frac{q}{m^*}\sqrt{\frac{\hbar}{2\epsilon\omega_\mathbf{q}V}}\sqrt{m_{\mathbf{q},\sigma}}\delta_{m_{\mathbf{q},\sigma}-1,n_{\mathbf{q},\sigma}}\langle\mathbf{k}_i|\hat{e}_{\mathbf{q},\sigma}\cdot\mathbf{p}e^{i\mathbf{q}\cdot\mathbf{r}}|\mathbf{k}_f\rangle +$$
$$-\frac{q}{m^*}\sqrt{\frac{\hbar}{2\epsilon\omega_\mathbf{q}V}}\sqrt{m_{\mathbf{q},\sigma}+1}\delta_{m_{\mathbf{q},\sigma}+1,n_{\mathbf{q},\sigma}}]\langle\mathbf{k}_i|\hat{e}_{\mathbf{q},\sigma}\cdot\mathbf{p}e^{-i\mathbf{q}\cdot\mathbf{r}}|\mathbf{k}_f\rangle$$

Given that $q = \frac{2\pi}{\lambda}$, where λ is on the order of 10μm, the wavefunction and r vary on the order of order of nanometers, therefore, we can approximate $\mathbf{q}\cdot\mathbf{r} \approx 0$

$$\langle i|H_{int}|f\rangle = -\frac{q}{m^*}\sqrt{\frac{\hbar}{2\epsilon\omega_\mathbf{q}V}}\sqrt{m_{\mathbf{q},\sigma}}\delta_{m_{\mathbf{q},\sigma}-1,n_{\mathbf{q},\sigma}}\hat{e}_{\mathbf{q},\sigma}\cdot\langle\mathbf{k}_i|\mathbf{p}|\mathbf{k}_f\rangle +$$
$$-\frac{q}{m^*}\sqrt{\frac{\hbar}{2\epsilon\omega_\mathbf{q}V}}\sqrt{m_{\mathbf{q},\sigma}+1}\delta_{m_{\mathbf{q},\sigma}+1,n_{\mathbf{q},\sigma}}\hat{e}_{\mathbf{q},\sigma}\cdot\langle\mathbf{k}_i|\mathbf{p}|\mathbf{k}_f\rangle$$

We have computed the photon part of the wavefunction; however, we still need to compute the spatial component of the wavefunction, which includes the entire wavefunction including the envelope and bloch wavefunctions.

$$\begin{aligned}\langle \mathbf{k}_i|\mathbf{e}\cdot\mathbf{p}|\mathbf{k}_f\rangle &= \hat{e}_{\mathbf{q},\sigma}\cdot\int d^3\mathbf{r}u^*_{v_i}(r)\frac{1}{\sqrt{S}}exp(-i\mathbf{k}^{(i)}_\perp\cdot r_\perp)F^*_i(z)\mathbf{p}u_{v_f}(r)\frac{1}{\sqrt{S}}exp(i\mathbf{k}^{(f)}_\perp\cdot r_\perp)F_f(z)\\ &= \hat{e}_{\mathbf{q},\sigma}\cdot\int d^3\mathbf{r}u^*_{v_i}(r)\frac{1}{\sqrt{S}}exp(-i\mathbf{k}^{(i)}_\perp\cdot r_\perp)F^*_i(z)\frac{1}{\sqrt{S}}exp(i\mathbf{k}^{(f)}_\perp\cdot r_\perp)F_f(z)\mathbf{p}u_{v_f}(r)+\\ &\qquad u^*_{v_i}(r)\frac{1}{\sqrt{S}}exp(-i\mathbf{k}^{(i)}_\perp\cdot r_\perp)F^*_i(z)u_{v_f}(r)\mathbf{p}\frac{1}{\sqrt{S}}exp(i\mathbf{k}^{(f)}_\perp\cdot r_\perp)F_f(z)\end{aligned}$$

Due to the periodicity and rapid variation of the bloch wavefunctions compared to the slowly varying envelope function, we can approximate the integrals

$$\begin{aligned}\langle \mathbf{k}_i|\mathbf{p}|\mathbf{k}_f\rangle \simeq \langle u_{v_i}(r)|\mathbf{p}|u_{v_f}(r)\rangle\int d^3\mathbf{r}\frac{1}{\sqrt{S}}exp(-i\mathbf{k}^{(i)}_\perp\cdot r_\perp)F^*_i(z)\frac{1}{\sqrt{S}}exp(i\mathbf{k}^{(f)}_\perp\cdot r_\perp)F_f(z)+\\ \langle u_{v_i}(r)|u_{v_f}(r)\rangle\int d^3\mathbf{r}\frac{1}{\sqrt{S}}exp(-i\mathbf{k}^{(i)}_\perp\cdot r_\perp)F^*_i(z)\mathbf{p}\frac{1}{\sqrt{S}}exp(i\mathbf{k}^{(f)}_\perp\cdot r_\perp)F_f(z)\end{aligned}$$

Reintroducing the dot product of the polarization and the momentum we get

$$\langle \mathbf{k}_i|\hat{e}_{\mathbf{q},\sigma}\cdot\mathbf{p}|\mathbf{k}_f\rangle = \langle u_{v_i}(r)|\hat{e}_{\mathbf{q},\sigma}\cdot\mathbf{p}|u_{v_f}(r)\rangle\frac{1}{S}\delta(k^{(i)}_\perp-k^{(f)}_\perp)\langle F_i(z)|F_f(z)\rangle+ \quad (2.40)$$

$$\langle u_{v_i}(r)|u_{v_f}(r)\rangle\frac{1}{S}\delta(k^{(i)}_\perp-k^{(f)}_\perp)(-i\hbar e_x k^f_x+-i\hbar e_y k^f_y)\langle F_i(z)|F_f(z)\rangle+\langle F_i(z)|e_z\cdot\mathbf{p}|F_f(z)\rangle \quad (2.41)$$

So the first term in equation (2.41) represents an interband transition for example between conduction and valence band. Furthermore, in an optical transition, the transverse k is conserved between transitions. For the case relevant to intraband transitions, i.e. bound conduction band states, the envelope functions between different states are orthogonal due to the hamiltonian. This yields the famous intersubband selection rule, where the polarization can only be in the z or growth direction.

$$\langle \mathbf{k}_i|\mathbf{e}\cdot\mathbf{p}|\mathbf{k}_f\rangle = \delta_{i,v}\delta(k^{(i)}_\perp-k^{(f)}_\perp)e_z\langle F_i(z)|p_z|F_f(z)\rangle \quad (2.42)$$

Furthermore by applying the commutation relation, we can write the momentum matrix element in a more familiar form in terms of a dipole moment.

$$\frac{i}{\hbar}[H_0, z] = \frac{p_z}{m^*} \tag{2.43}$$

$$\langle F_i(z)|p_z|F_f(z)\rangle = \frac{im^*}{\hbar}(E_f - E_i)\langle F_i(z)|z|F_f(z)\rangle \tag{2.44}$$

However, when using equation (2.42) one has to pay careful attention to the form of the operator and envelope function used. When including non parabolicity, the conduction envelope functions are not guaranteed to be orthonormal since the full solution to the Hamiltonian must take into account the sum of all the envelope functions and Bloch wavefunctions from all the bands. We will discuss this complication in the following section.

2.3.1 Dipole Moment with nonparabolicity

Due to nonparabolicity, we need to consider the envelope functions from the various valence bands in order to properly compute the dipole matrix element [11]. The exact definition and Hamiltonian used to derive the envelope functions is

$$\begin{pmatrix} E_c(z) & \sqrt{\frac{2}{3}}Pk_z & -\sqrt{\frac{1}{3}}Pk_z \\ -\sqrt{\frac{2}{3}}Pk_z & E_{lh}(z) & 0 \\ \sqrt{\frac{1}{3}}Pk_z & 0 & E_{so}(z) \end{pmatrix} \begin{pmatrix} F_c \\ F_{lh} \\ F_{so} \end{pmatrix} = E \begin{pmatrix} F_c \\ F_{lh} \\ F_{so} \end{pmatrix}$$

the p_z operator is actually the off-axis matrix elements, which originally were the result of the $\mathbf{k} \cdot \mathbf{p}$ in our original hamiltonian.

$$p_z = \begin{pmatrix} 0 & \sqrt{\frac{2}{3}}Pm_0 & -\sqrt{\frac{1}{3}}Pm_0 \\ -\sqrt{\frac{2}{3}}Pm_0 & 0 & 0 \\ \sqrt{\frac{1}{3}}Pm_0 & 0 & 0 \end{pmatrix}$$

We can express the light hole and split off envelope functions in terms of the conduction band envelope functions.

$$-\sqrt{\frac{2}{3}}Pp_zF_c = (E - E_{lh}(z))F_{lh} \tag{2.45}$$

$$\sqrt{\frac{1}{3}}Pp_zF_c = (E - E_{so}(z))F_{so} \tag{2.46}$$

The full expression for the optical matrix elements is

$$\langle\psi_i(z)|p_z|\psi_f(z)\rangle = \begin{pmatrix} F_c^{(i)} & F_{lh}^{(i)} & F_{so}^{(i)} \end{pmatrix} \begin{pmatrix} 0 & \sqrt{\frac{1}{3}}Pm_0 & -\sqrt{\frac{1}{3}}Pm_0 \\ -\sqrt{\frac{2}{3}}Pm_0 & 0 & 0 \\ \sqrt{\frac{1}{3}}Pm_0 & 0 & 0 \end{pmatrix} \begin{pmatrix} F_c^{(f)} \\ F_{lh}^{(f)} \\ F_{so}^{(f)} \end{pmatrix}$$

Fortunately, we can write a closed form expression for the optical matrix element, without having to compute all the valence envelope functions.

$$\langle\psi_i(z)|p_z|\psi_f(z)\rangle = \frac{1}{2}\langle F_c^{(i)}|p_z\frac{m_0}{m(E_i,z)} + \frac{m_0}{m(E_f,z)}p_z|F_c^{(f)}\rangle \tag{2.47}$$

In addition, the total wavefunction is normalized to one, not just the conduction band component. Therefore, the proper normalization is

$$\langle\phi_c|1 + \frac{2}{3}p_z\frac{|P|^2/m_0^2}{[E_{(i)} - E_{lh}(z)]^2}p_z + \frac{1}{3}p_z\frac{|P|^2/m_0^2}{[E_{(i)} - E_{so}(z)]^2}p_z|\phi_c\rangle = 1 \tag{2.48}$$

According to Sirtori [11] the use of standard dipole moment for computation is still valid and commonly overestimates $\approx$ 5-10 percent. Finally, we can write the total optical scattering rate for emission as

$$W_{ems}^{i\to f} = \frac{\pi q^2(m_{\mathbf{q},\sigma}+1)}{m^{*2}\epsilon\omega_{\mathbf{q}}V}e_z^2|p_z^{(i\to f)}|^2\delta(E_f - E_i + \hbar\omega_{\mathbf{q}}) \tag{2.49}$$

$$W_{ems}^{i\to f} = \frac{\pi q^2\omega_{\mathbf{q}}(m_{\mathbf{q},\sigma}+1)}{\epsilon V}e_z^2|z^{(i\to f)}|^2\delta(E_f - E_i + \hbar\omega_{\mathbf{q}}) \tag{2.50}$$

Where $p_z^{(i\to f)}$ and $z^{(i\to f)}$ are computed normally or by taking into account nonparabolicity by equation (2.47).

2.3.2 Spontaneous Emission Lifetime

From equation (2.50), we can define two individual rates, one that is dependent on the photon number (m) in the cavity and one that is independent. The former is stimulated emission, the

latter is spontaneous emission. Electrons can automatically emit a photon given a certain probability. However, our previous derivation assumes emission into a specific mode and polarization. To compute the total rate, we need to sum the total rates into all available modes ($\mathbf{q}$) and polarizations (σ).

$$W_{sp}^{i\to f} = \frac{\pi q^2 \omega_{\mathbf{q}}}{\epsilon V} e_z^2 |z^{(i\to f)}|^2 \delta(E_f - E_i + \hbar\omega_{\mathbf{q}}) \tag{2.51}$$

If we assume box resonator, then in q space the available states available are uniformly spaced discrete points. The density of q states is $1/(2\pi/L)^3$. In spherical coordinates.

$$\rho(\mathbf{q})d^3\mathbf{q} = \frac{d^3\mathbf{q}}{8\pi^3/V} = \frac{Vq^2 \sin\theta dq d\theta d\phi}{8\pi^3} \tag{2.52}$$

$$W_{i,f,tot}^{(sp)} = \int W_{i,f,mode}^{sp}(\mathbf{q})\rho(\mathbf{q})d^3\mathbf{q} = \frac{e^2}{\epsilon 8\pi^2}|z^{(i\to f)}|^2 \int\int\int \omega_q e_z^2 q^2 \sin\theta \delta(E_f - E_i + \hbar\omega_{\mathbf{q}}) dq d\theta d\phi \tag{2.53}$$

Assume we integrate such that one polarization is always normal to the z axis, and the other polarization lies in between the z and q axis. Therefore, $e_z^2 = \sin^2\theta$

$$W_{i,f,tot}^{(sp)} = \int W_{i,f,mode}^{sp}(\mathbf{q})\rho(\mathbf{q})d^3\mathbf{q} = \frac{e^2}{\epsilon 8\pi^2}|z^{(i\to f)}|^2 \int\int\int \omega_q q^2 \sin^3\theta \delta(E_f - E_i + \hbar\omega_{\mathbf{q}}) dq d\theta d\phi \tag{2.54}$$

The result is

$$W_{i,f,tot}^{(sp)} = \frac{e^2 n^3}{\epsilon 3\pi\hbar^4 c^3}|z^{(i\to f)}|^2 (E_i - E_f)^3 \tag{2.55}$$

$$W_{i,f,tot}^{(sp)} = \frac{e^2 n}{\epsilon_0 3\pi\hbar c^3}|z^{(i\to f)}|^2 w_{if}^3 \tag{2.56}$$

In the Mid-IR the total spontaneous emission rate at 5 μm is often on the order of $\tau_{i\to f}^{sp} \approx 20$ ns.

2.3.3 Stimulated Emission

In the case of stimulated emission, on the other hand, we compute the emission rate into a specific mode. For most laser cavities, there are usually one or two low loss modes where emitted photons can exist long enough for the stimulated emission rate to increase. This feedback loop between

emitted photons generating more photons is the basic concept behind a laser.

$$W_{if}^{st} = \frac{\pi q^2 \omega_{\mathbf{q}} m_{\mathbf{q},\sigma}}{\epsilon V} e_z^2 |z^{(i\to f)}|^2 \delta(E_f - E_i + \hbar\omega_{\mathbf{q}}) \tag{2.57}$$

However, due to relations with uncertainty, the energy level is not exactly discrete, but rather distributed over a range of energies. So often the delta function is replaced with a normalized lineshape function $g(E)dE = \frac{1}{h} g(\nu)dE$. Therefore,

$$W_{if}^{st} = \int \frac{\pi q^2 \omega_{\mathbf{q}} m_{\mathbf{q},\sigma}}{\epsilon V} e_z^2 |z^{(i\to f)}|^2 \delta(E_f - E_i + \hbar\omega_{\mathbf{q}}) \frac{1}{h} g(\nu) dE \tag{2.58}$$

$$W_{if}^{st} = \frac{\pi q^2 \omega_{\mathbf{q}} m_{\mathbf{q},\sigma}}{\epsilon V h} e_z^2 |z^{(i\to f)}|^2 g(\nu) \tag{2.59}$$

Expressing the number of photons in the mode using the field strength

$$I = \frac{c m_{\mathbf{q},\sigma} \hbar \omega_{\mathbf{q},\sigma}}{nV} \tag{2.60}$$

Therefore, we can rewrite the expression as

$$W_{if}^{st} = \frac{\lambda^2 I}{8\pi\hbar\omega n^2 t_{spont}} g(\nu) \tag{2.61}$$

The linewidth of the Lorentzian linewidth is determined from lifetime broadening [13]. However, there is a factor of 3 that is missing from equation (2.63), which accounts for the fact that for intersubband transitions, unlike atomic medium, all the dipole moments are aligned [14]. Therefore, we have

$$W_{if}^{st} = \frac{3\lambda^2 I}{8\pi\hbar\omega n^2 t_{spont}} g(\nu) \tag{2.62}$$

$$W_{if}^{st} = \frac{3\lambda^2 I}{8\pi\hbar\omega n^2 t_{spont}} \frac{\Delta\nu/2\pi}{(\nu - \nu_0)^2 + \Delta\nu/2)^2} \tag{2.63}$$

$$2\pi\Delta\nu = \Delta\omega = \frac{1}{\tau_f} + \frac{1}{\tau_i} + \frac{2}{T_2^*} \tag{2.64}$$

The linewidth factor can be understood by remembering that a finite exponential decay in time domain, when fourier transformed, yields a Lorentzian in frequency domain, whose width is determined by the decay. Where T_2^* represents the pure dephasing rate and τ_i and τ_f are state

lifetimes. For a more complete derivation of linewidth broadening due to coherent collection of classical oscillators see Siegman [13]. This linewidth broadening, as we will see when computing intersubband gain is critical and can be measured from the linewidth of spontaneous emission, which in the Mid-IR is ≈ 25 meV.

2.3.4 Intersubband Gain

Due to stimulated emission, photons emitted into a cavity mode, increase the intensity of that mode leading to gain or amplification. To calculate the gain, we compute the number of extra photons generated along the axis of the cavity. The power flux (W/m^2) of a wave in medium is related to the time average poytning vector.

$$P = \langle E \times H \rangle = \frac{1}{2}\epsilon_0 n e E_0^2 \tag{2.65}$$

We assume our waveguide has transverse dimensions of w and L. Therefore, the photon flux normal to the direction of propagation is

$$\Phi = \frac{1}{2}\epsilon_0 n e E_0^2 \frac{1}{\hbar\omega} wL \tag{2.66}$$

Therefore, the photon flux over a length dy along the direction of propagation is therefore

$$d\Phi = W_{21}^{(st)} n_2 w dy - W_{12}^{(st)} n_1 w dy \tag{2.67}$$

Where n_2, and n_1 are the sheet densities of electrons in level 2 and 1. We also note that the stimulated emission and absorption rates are equal. We define G as the increase in number of photons divided by the total number of photons present. [15]

$$\begin{aligned} G = \frac{d\Phi/dy}{\Phi} = W_{21}^{(st)} \frac{\hbar\omega}{IwL}(n_2 - n_1) &= \frac{3\lambda^2 I}{8\pi\hbar\omega n^2 t_{spont}} \frac{\hbar\omega w}{IwL}(n_2 - n_1) g(\nu) \\ G &= \frac{3\lambda^2}{8\pi n^2 t_{spont}} \frac{1}{L}(n_2 - n_1) g(\nu) \\ G &= \frac{1}{2n} \frac{e^2}{\epsilon_0 \hbar c} |z^{(i\to f)}|^2 w_{if} \frac{1}{L}(n_2 - n_1) g(\nu) \end{aligned}$$

For simplicity, we have assumed a low population density, such that we can assume that the final states of the electrons are free and available. We can also express the peak gain when $\nu = \nu_0$

$$G(\nu = \nu_0) = \frac{e^2|z^{(i\to f)}|^2 w_{if}}{2n\epsilon_0\hbar c}\frac{(n_2 - n_1)}{L}\frac{2}{\pi\Delta\nu} \tag{2.68}$$

$$G(\nu = \nu_0) = \frac{e^2|z^{(i\to f)}|^2 w_{if}}{n\epsilon_0 c}\frac{(n_2 - n_1)}{L}\frac{2}{\Delta E} \tag{2.69}$$

Where ΔE is the linewidth measured from spontaneous emission. However, the key factor is that the gain of a system is positive only when $n_2 > n_1$, or when one has a population inversion.

2.3.5 Nonradiative Scattering and Transitions

In quantum cascade lasers, population inversion is achieved by engineering the scattering rates and subband lifetimes. These subband and electronic populations are primarily controlled by nonradiative scattering mechanisms. There are a variety of nonradiative scattering mechanisms that are present in controlling electron transport including e-e scattering, acoustic phonon, electron impurity etc. For more detailed deviation and computational implementation for each of these scattering mechanisms see reference [16]. The mechanism that we will focus on primarily is polar longitudinal optical phonon scattering. This mechanism has a flat energy dispersion and for InGaAs is $\approx$ 34 meV. When subband levels are resonant with a LO phonon, the nonradiative scattering mechanism occurs on the order of 0.2 ps, which provides the main depopulation mechanism for various double phonon QCL designs. To compute the scattering rate due to LO phonon scattering we must again use Fermi's Golden Rule, with H_{int} is assumed to be [17]

$$H'_\beta = C\left[a_\beta e^{i\beta\cdot\mathbf{r}} + a^\dagger_\beta e^{-i\beta\cdot\mathbf{r}}\right] \tag{2.70}$$

$$C^2 = \frac{\hbar\omega_{LO}}{2V}\frac{e^2}{\beta^2}\left(\frac{1}{\epsilon_\infty} - \frac{1}{\epsilon_{DC}}\right) \tag{2.71}$$

As was the case for optical transitions, we can quantize the phonon motion, which assumes a certain phonon number, which are affected by the raising and lowering operators in equation (2.70)

$$W_{i\to f} = \frac{2\pi}{\hbar}|\langle i|H'_\beta|f\rangle|^2\delta(E_f - E_i \pm \hbar\omega_\beta) \tag{2.72}$$

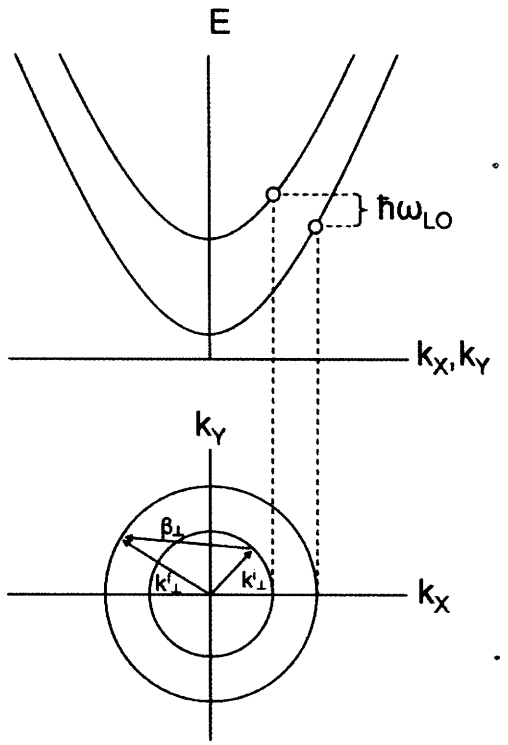

Figure 2-2: Diagram of LO phonon scattering between two parabolic subbands.

$$|i\rangle = |\mathbf{k}_i, n_\beta\rangle \tag{2.73}$$

$$|f\rangle = |\mathbf{k}_f, m_\beta\rangle \tag{2.74}$$

$$|\mathbf{k}_i\rangle = u_{v_i}(r)\frac{1}{\sqrt{S}}e^{i\mathbf{k}_\perp^{(i)}\cdot r_\perp}F_i(z) \tag{2.75}$$

Therefore the matrix element of Fermi's Golden Rule for just the case of emission or absorption is

$$|\langle i|H'_\beta|f\rangle|^2 = C^2\left(m_\beta + \frac{1}{2} \pm \frac{1}{2}\right)\left[\int d^3\mathbf{r}u^*_{v_i}(r)\frac{1}{\sqrt{S}}e^{-i\mathbf{k}_\perp^{(i)}\cdot r_\perp}F_i^*(z)e^{-i\beta\cdot\mathbf{r}}u_{v_i}(r)\frac{1}{\sqrt{S}}e^{i\mathbf{k}_\perp^{(i)}\cdot r_\perp}F_i(z)\right]^2$$

$$|\langle i|H'_\beta|f\rangle|^2 = C^2\left(m_\beta + \frac{1}{2} \pm \frac{1}{2}\right)\langle u^*_{v_i}(r)|u_{v_i}(r)\rangle\left[\int d^3\mathbf{r}e^{-i\mathbf{k}_\perp^{(i)}\cdot r_\perp}F_i^*(z)e^{-i\beta\cdot\mathbf{r}}e^{i\mathbf{k}_\perp^{(i)}\cdot r_\perp}F_i(z)\right]^2$$

$$|\langle i|H'_\beta|f\rangle|^2 = C^2\left(m_\beta + \frac{1}{2} \pm \frac{1}{2}\right)\delta_{\mathbf{k}_\perp^{(i)},\mathbf{k}_\perp^{(f)}\pm\beta_\perp}\left[\int F_i^*(z)e^{-i\beta_z z}F_i(z)dz\right]^2$$

The integration over the $k_\perp$ ensures transverse momentum conservation.

$$W_{i\to f}^{LO} = \frac{2\pi}{\hbar}\frac{\hbar\omega_{LO}e^2}{2V}\left(\frac{1}{\epsilon_\infty} - \frac{1}{\epsilon_{DC}}\right)\left(m_\beta + \frac{1}{2} \pm \frac{1}{2}\right)\frac{1}{\beta_\perp^2 + \beta_z^2} \times$$

$$\left[\int F_i^*(z)e^{-i\beta_z z}F_f(z)dz\right]^2 \delta_{\mathbf{k}_\perp^{(i)},\mathbf{k}_\perp^{(f)},\pm\beta_\perp}\delta(E_f - E_i \pm \hbar\omega_\beta)$$

In order to compute the total scattering rate out of $\mathbf{k}_i$ we must sum over all possible allowed final states $\mathbf{k}_f$ and allowed $(\beta_\perp, \beta_z)$. For simplicity let us look at the integration over β_z since it does not have any restrictions in terms of energy and momentum.

$$B_{i\to f}(\beta_\perp) = \int d\beta_z \frac{1}{\beta_\perp^2 + \beta_z^2}\int F_i^*(z)e^{-i\beta_z z}F_f(z)dz \int F_i(z')e^{i\beta_z z'}F_f^{*'}(z')dz' \tag{2.76}$$

$$= \int F_i^*(z)F_f(z)dz \int F_i(z')F_f^*(z')dz' \int d\beta_z \frac{1}{\beta_\perp^2 + \beta_z^2}e^{-i\beta_z(z-z')} \tag{2.77}$$

Fortunately, we can use a fourier transform pair to evaluate the integral β_z on the right.

$$B_{i\to f}(\beta_\perp) = \int F_i^*(z)F_i(z)dz \int F_i(z')F_i^*(z')dz' e^{-i\beta_\perp|z-z'|}\frac{1}{2\beta_\perp} \tag{2.78}$$

In order to integrate over the final states with allowed $\beta_\perp$, we can combine the conditions for energy and momentum conservation into

$$\beta_\perp^2 = k_i^2 + k_f^2 - 2k_i k_f \cos\theta \tag{2.79}$$

$$k_f^2 = k_i^2 + \frac{2m^*(\Delta_{fi} \mp \hbar\omega_{LO})}{\hbar^2} \tag{2.80}$$

$$\Delta_{fi} = E_f(k=0) - E_i(k=0) \tag{2.81}$$

Therefore, to satisfy energy and momentum conservation, we can integrate over θ, which is the angle between vectors $\mathbf{k}_i$ and $\mathbf{k}_f$.

$$W^{LO}(\mathbf{k_i}) = \frac{2\pi}{\hbar}\frac{\hbar\omega_{LO}e^2}{2V}\left(\frac{1}{\epsilon_\infty} - \frac{1}{\epsilon_{DC}}\right)\left(m_\beta + \frac{1}{2} \pm \frac{1}{2}\right)\int_0^{2\pi} d\theta B_{i\to f}(\beta_\perp) \tag{2.82}$$

To account for phonon statistics we can assume Bose Einstein distribution functions that are in equilibrium with the lattice temperature. We have also included figure 2-3 to show the effects of detuning the subband separation given fixed wavefunctions.

$$m_\beta = \frac{1}{e^{\frac{E-\mu_{LO}}{kT_l}} - 1} \tag{2.83}$$

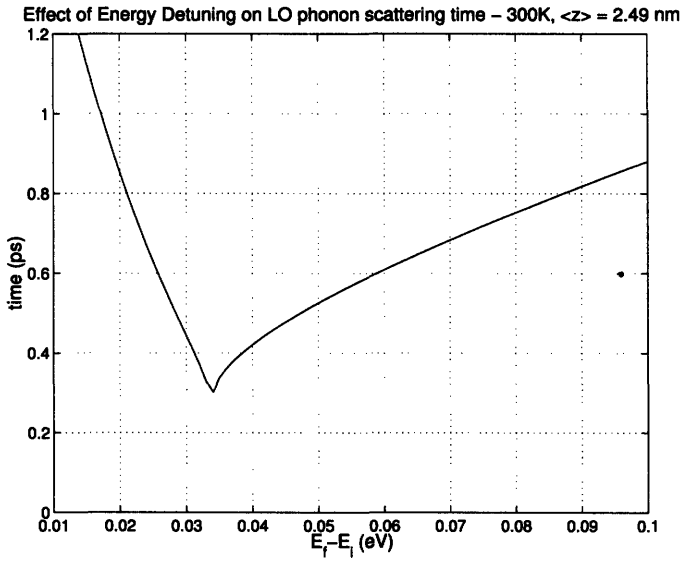

Figure 2-3: Effect of Detuning between subbands versus scattering time

2.4 Resonant Tunneling

So far transport of electrons has assumed a coherent process where electrons due to specific scattering mechanisms can scatter from one subband to another. However, it has been shown that this coherent process of transport, at least between modules, may not be entirely accurate. In quantum cascade lasers describing the transport between modules is often treated using resonant tunneling [18]. Experimentally this is shown through the strong dependence of injection barrier thickness to current density. For coherent transport when two levels align, the wavefunction assumes a spatially delocalized state across the barrier and thus has some large spatial overlap with subbands in the next module. Therefore the injection barrier would have little affect on the total current passing through the barrier. Furthermore, dephasing due to transport accross a barrier is critical for QCL performance. Modeling of dephasing can most easily be done through Density Matrix Formalism.

2.4.1 Density Matrix Formalism

For an arbitrary electron wavefunction

$$|\psi\rangle = \sum_n c_n |\phi_n\rangle \tag{2.84}$$

Where ϕ_n are the basis states of the Hamiltonian. If one were to compute the expectation value of an operator then

$$\langle\psi|O|\psi\rangle = \sum_m \sum_n c_m^* c_n \langle\phi_m|O|\phi_n\rangle = \sum_m \sum_n c_m^* c_n O_{mn} \tag{2.85}$$

Let us define the density operator ρ and density matrix ρ_{nm}

$$\rho = |\psi\rangle\langle\psi| = \sum_m \sum_n c_n^* c_m |\phi_m\rangle\langle\phi_n| \tag{2.86}$$

$$\rho_{nm} = \langle\phi_m|\rho|\phi_n\rangle = c_n^* c_m \tag{2.87}$$

$$\rho_{nm} = \langle\phi_m|\rho|\phi_n\rangle = \langle c_n^* c_m\rangle \tag{2.88}$$

Therefore, for a single particle we can express the wavefunction in this density matrix formalism. However, for our purpose the density matrix through averaging many different single density matrices can represent an ensemble average, which allows us to model large collections of electrons at once assuming some mean behavior, which is the true strength of this formalism. Therefore, the expression for the expectation can be written as

$$\langle O\rangle = \sum_m \sum_n \rho_{nm}^* O_{mn} = \sum_m \sum_n \rho_{mn} O_{mn} \tag{2.89}$$

Furthermore, the density matrix is Hermitian

$$\rho_{nm}^* = \langle\phi_m|\rho|\phi_n\rangle^* = (c_n^* c_m)^* = c_m^* c_n = \rho_{mn} \tag{2.90}$$

By taking the time derivative of the density operator we arrive at the time evolution of the density matrix.

$$i\hbar\frac{\partial\rho}{\partial t} = i\hbar\frac{\partial|\psi\rangle}{\partial t}\langle\psi| + i\hbar|\psi\rangle\frac{\partial\langle\psi|}{\partial t} \tag{2.91}$$

$$i\hbar\frac{\partial\rho}{\partial t} = H|\psi\rangle\langle\psi| - |\psi\rangle\langle\psi|H = [\rho, H] \tag{2.92}$$

For clarity, let us only consider a situation where we only have two basis states. Furthermore, we have assumed our $H_{tot} = H + H_{relax}$, where H_{relax} includes phenomenological relaxation processes such as dephasing or population lifetimes, that are difficult to write out explicitly in

terms of a Hamiltonian.

$$\frac{\partial}{\partial t}\begin{pmatrix} \rho_{11} & \rho_{12} \\ \rho_{21} & \rho_{22} \end{pmatrix} = \left[\begin{pmatrix} \rho_{11} & \rho_{12} \\ \rho_{21} & \rho_{22} \end{pmatrix}, \begin{pmatrix} H_{11} & H_{12} \\ H_{21} & H_{22} \end{pmatrix}\right] + \frac{\partial \rho}{\partial t}_{relax}$$

For the case relevant for resonant tunneling, assume initially we have two isolated quantum wells with a very thick barrier. The initial basis states would naturally be $|\phi_1\rangle$ and $|\phi_2\rangle$, which are localized states inside the well. Assume the Hamiltonian for a single well is H_0 then the coupling between the two wells can be viewed as a perturbation ΔV, so the $H = H_0 + \Delta V$. Therefore,

$$H = \begin{pmatrix} \langle\phi_1|H|\phi_1\rangle & \langle\phi_1|H|\phi_2\rangle \\ \langle\phi_2|H|\phi_1\rangle & \langle\phi_2|H|\phi_2\rangle \end{pmatrix} = \begin{pmatrix} E_1 & \langle\phi_1|\Delta V|\phi_2\rangle \\ \langle\phi_2|\Delta V|\phi_1\rangle & E_1 \end{pmatrix} = \begin{pmatrix} E_1 & -\Delta_0/2 \\ -\Delta_0/2 & E_1 \end{pmatrix}$$

The eigenfunctions of this matrix now form delocalized states that are symmetric and antisymmetric which are separated in energy by their anticrossing strength Δ_0. However, with QCL's two states can be brought into resonance through an applied electric field. Therefore assuming fixed anticrossing strength, we allow detuning, such that the diagonal elements of the matrix can differ.

$$H = \begin{pmatrix} E_1 & -\Delta_0/2 \\ -\Delta_0/2 & E_2 \end{pmatrix}$$

Furthermore, it becomes clear that if an electron is originally in one of these localized basis states, that it is not a eigenfunction of the Hamiltonian and will undergo oscillations between the two basis states, thus allowing tunneling across the barrier. Density matrix formalism also allows the ability to add in ensemble parameters, such as population lifetimes and dephasing phenomenologically.

$$\frac{\partial \rho}{\partial t}_{relax} = \begin{pmatrix} \frac{\rho_{22}}{\tau} & \frac{\rho_{12}}{\tau_{||}} \\ \frac{\rho_{21}}{\tau_{||}} & -\frac{\rho_{22}}{\tau} \end{pmatrix}$$

For simplicity, we assume a infinite periodic lattice. We define a lifetime τ as the lifetime of ρ_{22} where an electron relaxes from 2 into 1. We also define $\tau_{||}$ as the dephasing relaxation time due to loss of coherence between the two wavefunctions. If current is directly injected into level 2, then the steady state current density $J = \frac{qN\rho_{22}}{\tau}$. If we solve equation (2.92) for ρ_{22} under the condition that $\rho_{22} + \rho_{11} = 1$ assuming a constant population, we can express the current in a

form similar to the one provided by Karzarinov and Sirus [6].

$$J = \frac{qN\rho_{22}}{\tau} = \frac{qN}{2}\frac{\left(\frac{\Delta_0}{\hbar}\right)^2 \tau_{||}}{1+\left(\frac{E_{21}}{\hbar}\right)^2 \tau_{||}^2 + \left(\frac{\Delta_0}{\hbar}\right)^2 \tau\tau_{||}} \tag{2.93}$$

This expression can be simplified for the case where the two energy levels are resonant.

$$J_{max} = \frac{qN}{2}\frac{\left(\frac{\Delta_0}{\hbar}\right)^2 \tau_{||}}{1+\left(\frac{\Delta_0}{\hbar}\right)^2 \tau\tau_{||}} \tag{2.94}$$

We can estimate $\tau_{||}$ from homogeneous broadening of the linewidth similar to equation (2.64).

$$\frac{1}{\tau_{||}} = \frac{1}{\tau} + \frac{2}{T_2^*} \tag{2.95}$$

$$\Delta\omega_0 = \frac{1}{T_2} \approx \frac{1}{\tau_{||}} \tag{2.96}$$

For a linewidth on the order of 25-50 meV this corresponds to a dephasing rate $\approx$ 100 fs. It should be noted that the measured emission linewidth is the transition within a well, where as the linewidth in question is the transport across a barrier, which one would expect to be broader; however, this is an unknown parameter in the system.

The resonant tunneling model provides a a figure of metric when designing optimal device performance of a QCL. Following from [18], the optimal strong coupling regime, where $|\frac{\Delta_0}{\hbar}|^2\tau\tau_{||} \gg 1$, is preferred such that

$$J_{max} = \frac{qN}{2\tau} \tag{2.97}$$

We see that the current is limited not by the tunneling rate, but by the lifetime τ, which means more electrons are available for gain. Therefore in designing QCL's careful attention must be paid to the various anticrossing between levels to determine the injector coupling strength.

2.5 Rate Equations for QCL

After deriving optical and nonradiative scattering mechanisms, we can use rate equations to determine what parameters are important for population inversion. As is done with many laser systems we reduce the QCL down to a simple three level system [14] [19]. Through detailed

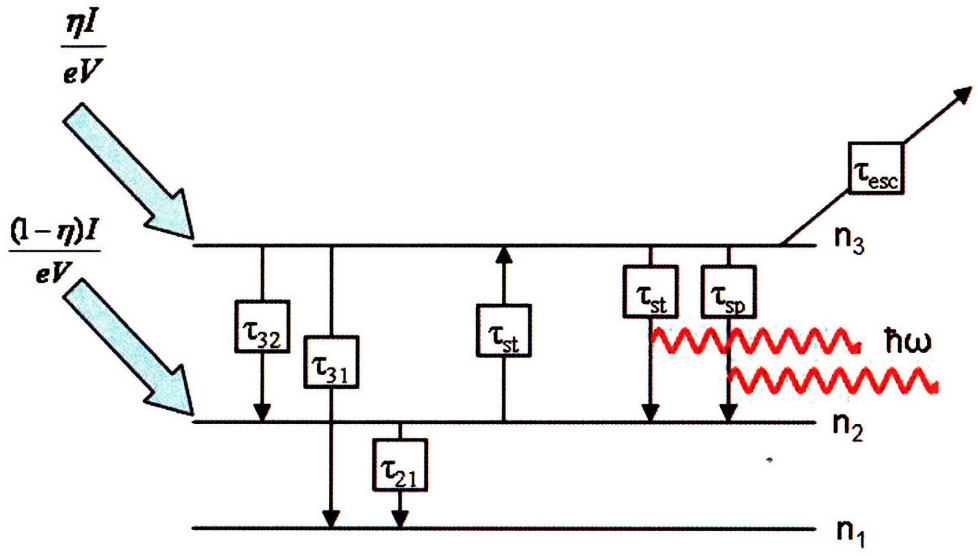

Figure 2-4: Diagram of Three Level system, assuming non unity injection efficiency

balance, we can write down the rate equations for the 3-D subband populations n_3 and n_2. We can even keep track of the number of photons in a specific lasing cavity by including terms such as spontaneous and stimulated emission and absorption.

$$\frac{dn_3}{dt} = \frac{\eta I}{eV} - \frac{n_3}{\tau_{sp}} + \frac{(n_2 - n_3)mV}{\tau_{st}} - \frac{n_3}{\tau_3} \tag{2.98}$$

$$\frac{dn_2}{dt} = \frac{(\eta - 1)I}{eV} + \frac{n_3}{\tau_{sp}} + \frac{(n_3 - n_2)mV}{\tau_{st}} - \frac{n_2}{\tau_2} + \frac{n_3}{\tau_{32}} \tag{2.99}$$

$$\frac{dm}{dt} = \frac{n_3\Gamma}{\tau_{sp}} + \frac{(n_3 - n_2)\Gamma mV}{\tau_{st}} - \frac{m}{\tau_p} \tag{2.100}$$

We assumed that current I is directly injected into level 3, V is the volume of the active region, η injection efficiency, τ_p is the photon lifetime, Γ is the confinement factor.

$$\tau_p = \frac{1}{v_g(\alpha_m + \alpha_w)} \tag{2.101}$$

$$\Gamma = \frac{VN_{mod}}{V_{tot}} \tag{2.102}$$

$$\frac{1}{\tau_3} = \frac{1}{\tau_{32}} + \frac{1}{\tau_{31}} + \frac{1}{\tau_{esc}} \tag{2.103}$$

Where V_{tot} is the total cavity volume, and the $n_3 = n_3^{2D}/L_{mod}$ and $n_2 = n_2^{2D}/L_{mod}$. Now assume steady state conditions.

$$\frac{\eta I}{eV} = \frac{n_3}{\tau_{sp}} - \frac{(n_2 - n_3)mV}{\tau_{st}} + \frac{n_3}{\tau_3} \tag{2.104}$$

$$\frac{(\eta - 1)I}{eV} = -\frac{n_3}{\tau_{sp}} - \frac{(n_3 - n_2)mV}{\tau_{st}} + \frac{n_2}{\tau_2} - \frac{n_3}{\tau_{32}} \tag{2.105}$$

$$\frac{n_3\Gamma}{\tau_{sp}} + \frac{(n_3 - n_2)\Gamma mV}{\tau_{st}} = \frac{m}{\tau_p} \tag{2.106}$$

For simplicity, we assume that $\tau_{sp} \gg \tau_{st}$ and there are a large number of photons in the active region such that $mV \gg 1$. From equation (2.106)

$$n_3 - n_2 = \frac{\tau_{st}}{\tau_p}\frac{1}{\Gamma V} \tag{2.107}$$

For conditions above threshold, equation (2.107) demonstrates that the population inversion or gain clamps above threshold. We can solve equations (2.105) and (2.104) for the photon number (m) which is proportional to Light Intensity (L) assuming the fixed population inversion.

$$m = \frac{\tau_p\Gamma(\eta\tau_3(1 - \tau_2/\tau_{32}) - (1 - \eta)\tau_2)}{\tau_2 + \tau_3(1 - \tau_2/\tau_{32})}(P - P_{th}) \tag{2.108}$$

$$P_{th} = \frac{\tau_{st}}{\tau_p V\Gamma}\frac{1}{\eta\tau_3(1 - \tau_2/\tau_{32}) - (1 - \eta)\tau_2} \tag{2.109}$$

$$L = \frac{\hbar\omega V_p m}{\tau_m} \tag{2.110}$$

$$\tau_m = \frac{1}{\alpha_m v_g} \tag{2.111}$$

Where $P = \frac{I}{eV}$. Finally expressing equation (2.108) in terms of L, we can express the slope efficiency $\frac{dL}{dI}$ or the amount of output power versus current.

$$\frac{dL}{dI} = \frac{\hbar\omega V_p}{eV\tau_m}\frac{\tau_p\Gamma(\eta\tau_3(1 - \tau_2/\tau_{32}) - (1 - \eta)\tau_2)}{\tau_2 + \tau_3(1 - \tau_2/\tau_{32})} \tag{2.112}$$

$$\frac{dL}{dI} = \frac{\hbar\omega N_{mod}}{e}\frac{\alpha_m}{\alpha_m + \alpha_w}\frac{(\eta\tau_3(1 - \tau_2/\tau_{32}) - (1 - \eta)\tau_2)}{\tau_2 + \tau_3(1 - \tau_2/\tau_{32})} \tag{2.113}$$

$$\tag{2.114}$$

These results will be useful for deriving expression for evaluating wall plug efficiency.

2.5.1 Wall Plug Efficiency

Quantum cascade lasers have a distinctive advantage of being able to engineer the scattering mechanisms between levels by tailoring their energy separations as well as their wavefunctions. From equation (2.114), it is clear that the scattering times $\tau_{32}, \tau_3, \tau_2$ are very important for high efficiency. For determining all the factors relevant for wall plug efficiency, Jerome Faist derives an expression for fundamental wall plug efficiency η_{wp} [20].

$$\eta_{wp} = \frac{(I - I_{th})dL/dI}{IV} \tag{2.115}$$

Where V is the voltage to bias the device, I is the current, I_{th} is the threshold current. We can relate the parameters V for a specific device wavelength as

$$V = \left(\frac{\hbar\omega}{q_0} + \Delta_{inj}\right) N_{mod} \tag{2.116}$$

Where Δ_{inj} is the voltage defect to bring the various levels into alignment beyond the necessary energy alignment separation between the upper and lower lasing state. Traditionally, depending on design this can vary from 70 meV for the injectorless to 120 meV for the traditional miniband designs. The voltage defect is due to the need for extra levels to provide depopulation. Using rate equation solutions, Faist simplified the wall plug efficiency down to a concise expression

$$\eta_{wp,max} = \frac{\tau_{32} - \tau_2}{\tau_{32} + \tau_{32}\tau_2/\tau_3 - \tau_2} \frac{1}{1 + \Delta_{inj}/(\hbar\omega)} \left[\frac{\sqrt{g^*\tau^*} - 1}{\sqrt{g^*\tau^*}}\right]^2 \tag{2.117}$$

$$\tau^* = \frac{\tau_3(1 - \tau_2/\tau_{32})}{\tau_{trans}} \tag{2.118}$$

$$g^* = \frac{m^*\omega^3\tau_{||}\tau_{fc}}{\hbar}|z_{i\to f}|^2 \tag{2.119}$$

$$J_{max} = \frac{n_s q_0}{\tau_{trans}} \tag{2.120}$$

It becomes very clear that the parameters that need to be optimized are $\sqrt{g^*\tau^*} \gg 1$. Some of these parameters such as $\tau_{||}$ are controlled by the growth and quality of the interfaces, which affect the linewidth. However, most of the other parameters in terms of lifetimes and voltage defects are parameters that are dependent on the design. Therefore, for this thesis we will further explore various injectorless designs for reducing Δ_{ij}.

Chapter 3

Simulations

Monte Carlo simulations were conducted for evaluating and studying various designs. Various simulation tools have been developed to study and model electron transport in quantum cascade structures. Most simulations for QCL's involve a semiclassical approach which is essentially a rate equation approach, where electrons in different subbands scatter into and out of different levels. A Monte Carlo approach is often taken to simulate ensemble electron behavior. These simulations were done on two designs to evaluate the performance of using these simulations for predicting the performance of new designs

3.1 Monte Carlo

A common method for simulating electron transport in semiconductor devices is a Monte Carlo simulation. By following the Boltzman Transport Equations [17], electrons are assumed to be discrete particles with known momentum and energy. Electrons once inside a material can be subject to a variety of scattering mechanism such as optical phonon scattering, interface scattering, impurity scattering etc. Each of these scattering mechanisms is assumed to be instantaneous and obey transverse momentum and energy conservation. The choice of scattering event is determined by the probability of each scattering mechanism. Allowing random events to choose the scattering event is where the simulation gets its name. The results of the simulation can yield information about final steady state populations, gain, electron temperatures, scattering rates, and current. The code used was developed by Hans Callebaut initially for simulating terahertz QCL. It was then modified slightly to take into account nonparabolicity for solving

mid-IR QCL structures.

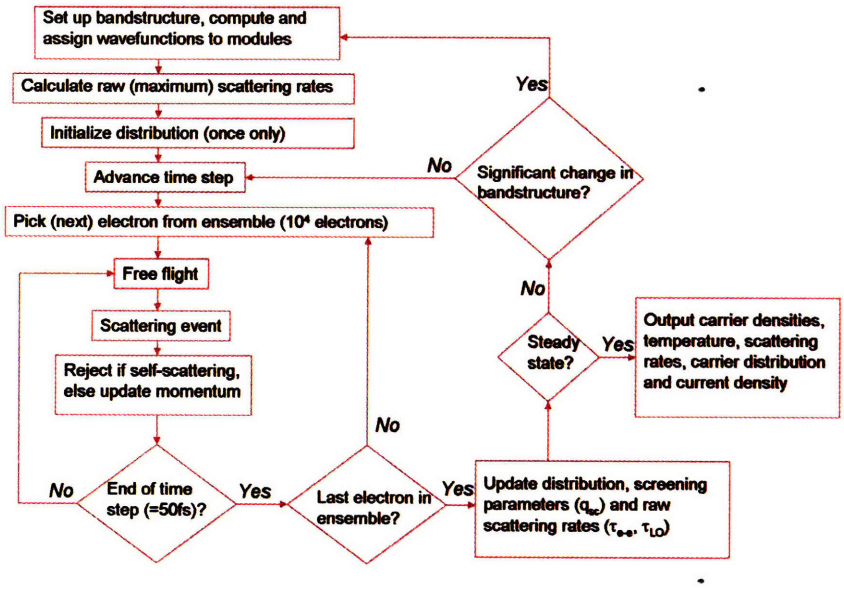

Figure 3-1: Flow Chart for Monte Carlo Simulation

3.1.1 Free Flight

After computing the band structure, the Monte Carlo simulation must determine for each individual electron the time between scattering events. The probability distributions are determined by the relative strengths of the scattering rates computed using Fermi's Golden Rule. Furthermore, each electron themselves is modeled with a specific $\mathbf{k}_\perp$ and subband (i).

$$\Gamma^i(\mathbf{k}_\perp, t) = \sum_m \frac{1}{\tau_m^i(\mathbf{k}_\perp, t)} \tag{3.1}$$

Where m is the scattering mechanism and Γ is the total scattering rate. For simplicity, we assume $\Gamma^i(\mathbf{k}_\perp, t) = \Gamma_0$ [17]. Electrons in the system are assumed to undergo free flight until a scattering mechanism is chosen. If we define n_{cf} as the number of electrons which have not undergone a collision since time t=0, then assuming a scattering rate of Γ_0,

$$\frac{dn_{cf}}{dt} = -\Gamma_0 n_{cf} \tag{3.2}$$

$$\frac{n_{cf}(t)}{n_{cf}(0)} = e^{-\Gamma_0 t} \tag{3.3}$$

Equation (3.3) defines the probability that an electron has not scattered until time t. Therefore since Γ_0 is the number of electrons scattering per second, we know that the the number of electrons that scatter in time interval dt is $\Gamma_0 dt$. The probability that an electron undergoes its first scattering between t and dt is the multiplication of the probability it has not scattered until time t and the probability of scattering in time interval dt.

$$P(t)dt = \Gamma_0 e^{-\Gamma_0 t} dt \tag{3.4}$$

For computational reasons, we would like to map the probability distribution P(t) onto a uniform probability distribution P(r)

$$\begin{aligned} P(r)dr &= P(t)dt & (3.5)\\ dr &= \Gamma_0 e^{-\Gamma_0 t} dt & (3.6)\\ \int_0^{r_c} dr &= \int_0^{t_c} \Gamma_0 e^{-\Gamma_0 t} dt & (3.7) \end{aligned}$$

Where solving equation (3.7) is a simple map between a uniform probability distribution (r_c) and a time duration for free flight (t_c).

$$t_c = -\frac{1}{\Gamma_0} ln(1 - r_c) \tag{3.8}$$

This assumption is of course assumes a constant scattering rate; however, this can be artificially introduced into the Monte Carlo simulation by introducing a fictitious self-scattering event.

$$\Gamma^i_{self}(\mathbf{k}_\perp, t) = \Gamma_0 - \Gamma^i(\mathbf{k}_\perp, t) \tag{3.9}$$

This self scattering event, if chosen, does not change an electrons energy or momentum.

3.1.2 Choosing a Scattering Mechanism

Every particle due to its energy and momentum has its own unique probability of scattering. The process for choosing which scattering mechanism an electron undergoes and the corresponding

change in energy and momentum are chosen according to

$$\frac{\sum_{m=1}^{l-1} \frac{1}{\tau_m^i(\mathbf{k}_\perp,t)}}{\Gamma_0} \leq r_2 < \frac{\sum_{m=1}^{l} \frac{1}{\tau_m^i(\mathbf{k}_\perp,t)}}{\Gamma_0} \tag{3.10}$$

$$\frac{\sum_{i=1}^{j-1} \frac{1}{\tau_m^i(\mathbf{k}_\perp,t)}}{\Gamma_0} \leq r_3 < \frac{\sum_{i=1}^{j} \frac{1}{\tau_m^i(\mathbf{k}_\perp,t)}}{\Gamma_0} \tag{3.11}$$

Where r_2 and r_3 are random numbers chosen from a uniform probability distribution. r_2 selects the scattering mechanism and r_3 given the scattering mechanism chosen selects the appropriate subbands that the electrons will scatter into. For a more complete and in depth description over implementation of the various scattering mechanisms such as e-e and e-imp, refer to [16]. After choosing an appropriate subband, the final subband may not be within the QCL module. In this case periodic boundary conditions are imposed in a similar fashion done by Iotti and Rossi [21]. In the simulations, traditionally 3 QCL modules are simulated at a time, but electrons are only tracked in the center module. Electrons that scatter to adjacent modules are reinjected back into the center module with the appropriate momentum and energy. Using this approach, values such as current density can be computed simply as the flux of electrons passing into the next module.

3.1.3 Shooting Method

For computing the electronic wavefunctions, the shooting method was implemented to solve for the appropriate eigenfunctions and eigenvalues [22]. The shooting method first discretizes equation (2.22) and (2.23)

$$\frac{\psi[z+\Delta z]}{m^*[z+\Delta z/2]} = \left[\frac{2(\Delta z)^2}{\hbar^2}[V(z)-E] + \frac{1}{m^*[z+\Delta z/2]} + \frac{1}{m^*[z-\Delta z/2]}\right]\psi(z) - \frac{\psi[z-\Delta z]}{m^*[z-\Delta z/2]} \tag{3.12}$$

In order to write the effective mass in terms of more familiar parameters such as band gap and band edge effective mass

$$m(E,z) = m^*(z)\left(1 + \frac{E-V(z)}{E_g(z)}\right) \tag{3.13}$$

We can also show that the form of equation (3.12) satisfies the appropriate boundary conditions at the interface. Let $\Delta z \rightarrow 0$, in equation (3.12).

$$\frac{\psi[z+\Delta z]}{m^*[E,z+\Delta z/2]} = \left[\frac{1}{m^*[E,z+\Delta z/2]} + \frac{1}{m^*[E,z-\Delta z/2]}\right]\psi[z] - \frac{\psi[z-\Delta z]}{m^*[E,z-\Delta z/2]} \tag{3.14}$$

$$\lim_{\Delta z \rightarrow 0} \frac{1}{\Delta z}\frac{\psi[z+\Delta z]-\psi[z]}{m^*[E,z+\Delta z/2]} = \frac{1}{\Delta z}\frac{\psi[z]-\psi[z-\Delta z]}{m^*[E,z-\Delta z/2]} \tag{3.15}$$

$$\frac{1}{m^*(E,z)^+}\frac{\partial\psi^+(z)}{\partial z} = \frac{1}{m^*(E,z)^-}\frac{\partial\psi^-(z)}{\partial z} \tag{3.16}$$

Therefore, equation (3.12) provides a difference equation given two initial data points for computing the rest of the wavefunction. Obviously, this will yield wavefunction solutions for any arbitrary energy value. Therefore, to solve for the correct solutions, the shooting method looks for solutions that fit the appropriate boundary conditions for bounded wavefunctions $\psi(\pm\infty) = 0$. Unfortunately, to computationally deal with ∞,we place our quantum well structure inside a larger infinite square potential. Therefore, eigenfunctions of the system will be solutions that go to zero at the boundaries of the square potential.

3.1.4 Material Parameters

As we will address later, QCL structures in order to achieve better confinement are composed of strained material systems, which are not lattice matched to the substrate. Unfortunately, parameters for strained ternary material systems are not well known including band offsets and effective masses. In order to estimate various material parameters, we used an interpolation scheme with bowing parameters from binary compounds [23].

$$P(a_{1-x}b_x) = (1-x)P_a + xP_b - x(1-x)B_{ab} \tag{3.17}$$

Where P is the property of interest, a and b are the different materials, B is the bowing parameter, x is percentage of material b. The Energy gap in table 3.1 follows the empirical varshni form

$$E_g(T) = E_g(T=0) - \frac{\alpha T^2}{T+\beta} \tag{3.18}$$

Table 3.1: Table of Material Parameters

	GaAs	InAs	AlAs
$a_{lc}(\mathring{A})(T = 300K)$	5.65325	6.0583	5.6611
$m_e^*(\Gamma)$	0.067	0.026	0.15
$E_g^\Gamma(T = 0)(eV)$	1.519	0.417	3.099
$\alpha(\Gamma)(meV/K)$	0.5405	0.276	0.885
$\beta(\Gamma)(K)$	204	93	530
$\Delta_{so}(eV)$	0.341	0.39	0.28
VBO (eV)	-0.80	-0.59	-1.33

Table 3.2: Bowing Parameters for InGaAs, InAlAs

	InGaAs	InAlAs
$a_{lc}(\mathring{A})(T = 300K)$	—	—
$m_e^*(\Gamma)$	0.0091	0.049
$E_g^\Gamma(T = 0)(eV)$	0.477	0.70
$\alpha(\Gamma)(meV/K)$	—	—
$\beta(\Gamma)(K)$	—	—
$\Delta_{so}(eV)$	0.15	0.15
VBO (eV)	-0.38	-0.64

For our expression for the effective mass in equation (3.13), we need the effective mass and the energy gap for the materials used, which in our case is InGaAs and InAlAs.

$$E_g^{v,avg}(\Gamma) = E_g^\Gamma + \frac{1}{3}\Delta_{so} \tag{3.19}$$

From interpolation, we have included some of the common material systems used in both injectorless and miniband designs. Where in terms of the energy interpolation, we have adopted

Table 3.3: Various InGaAs Material Parameters after Interpolation

In(x)Ga(1-x)As	$a_{lc}(\mathring{A})$ T=300K	$m_e^*(\Gamma)$	$E_g^{v,avg}(\Gamma)(eV)$ T=300K	$E_{v,av}^{abs}$ (eV)	Cite
x = 0.600	5.8963	0.0402	0.8548	-6.7621	[2],[24],[25]
x = 0.660	5.9206	0.0379	0.7978	-6.7476	[26]
x = 0.670	5.9246	0.0375	0.7888	-6.7452	[3]
x = 0.678	5.9279	0.0372	0.8903	-6.7433	[27],[28]

Table 3.4: Various InAlAs Material Parameters after Interpolation

In(x)Al(1-x)As	$a_{lc}(\AA)$ T=300K	$m_e^*(\Gamma)$	$E_g^{v,avg}(\Gamma)(eV)$ T=300K	$E_{v,av}^{abs}$ (eV)	Cite
x = 0.300	5.7803	0.1025	2.2412	-6.8379	
x = 0.346	5.7985	0.0960	2.1073	-6.8259	[26]
x = 0.362	5.8049	0.0938	2.0615	-6.8218	[3]
x = 0.365	5.8061	0.0934	2.0529	-6.8210	[2], [27],[28]
x = 0.440	5.8359	0.0834	1.8435	-6.8018	[24],[25]

a more complex bowing parameter that is strain dependent [29]

$$E(x) = xE(AC) + (1-x)E(BC) + 3x(1-x)[-a_i(AC) + a_i(BC)]\frac{\Delta a}{a_0} \tag{3.20}$$

where $\Delta a = a_0(AC) - a_0(BC)$ The last critical parameter for simulation is the Conduction Band Offset (CBO). There does not exist a systematic way to predict conduction band alignments for various material including strain. The most commonly used theory is from model solid theory [29]. Model Solid Theory assumes two aspects: one is an accurate band structure which can be solved using a variety of methods such as psuedopotentials, etc. The other aspects is defining an absolute energy scale with which to compare various energy alignments between different materials. Model solid theory addresses this by relating the average electrostatic potential to the vacuum level. A common reference point is accomplished by modeling the solid as a superposition of neutral atoms. The energy values in table 3.3 and 3.4 are interpolated using equation (3.20).

Including the deformation potentials further allows us to take into account strain induced effects for changing various band edges.

$$\Delta E_c = a_c(\epsilon_{xx} + \epsilon_{yy} + \epsilon_{zz}) \tag{3.21}$$

$$\Delta E_{v,avg} = a_v(\epsilon_{xx} + \epsilon_{yy} + \epsilon_{zz}) \tag{3.22}$$

Where a_c and a_v are the conduction and valence band deformation potentials, also we define the strain in the xx and yy directions as the transverse directions perpendicular to the growth direction zz. For the QCLs of interest we assume our substrate material is InP (001). The strain

induced in the InGaAs and InAlAs layers is caused by the lattice constant difference from InP.

$$a_{xx} = a_{sub} \tag{3.23}$$

$$a_{yy} = a_{sub} \tag{3.24}$$

$$a_{zz} = a_0 \left[1 - D^{001}\left(\frac{a_{sub}}{a_0} - 1\right)\right] \tag{3.25}$$

$$D^{001} = 2\frac{c_{12}}{c_{11}} \tag{3.26}$$

Where we have assumed that InP has a lattice constant of 5.8697 Å. We define the strain therefore as

$$\epsilon_i = \frac{a_i}{a_0} - 1, i \in (xx, yy, zz) \tag{3.27}$$

For common Mid-IR materials, we have already computed the various interpolated parameters for barrier and well materials.

In(x)Al(1-x)As	$a_{lc}(\AA)$ T=300K	$C12/C11$	$a_c(eV)$	$a_v(eV)$	$\frac{\Delta\Omega}{\Omega}$	ΔE_c	ΔE_v
x = 0.300	5.7803	0.4530	-5.1780	-2.0290	0.01693	-0.08765	-0.03435
x = 0.346	5.7985	0.4575	-5.1294	-1.9614	0.01332	-0.06831	-0.02612
x = 0.362	5.8049	0.4591	-5.1139	-1.9379	0.01208	-0.06177	-0.02341
x = 0.365	5.8061	0.4594	-5.1111	-1.9335	0.01185	-0.06056	-0.02291
x = 0.440	5.8359	0.4671	-5.0486	-1.8232	0.00618	-0.03119	-0.01126

In(x)Ga(1-x)As	$a_{lc}(\AA)$ T=300K	$C12/C11$	$a_c(eV)$	$a_v(eV)$	$\frac{\Delta\Omega}{\Omega}$	ΔE_c	ΔE_v
x = 0.600	5.8963	0.5039	-6.5424	-1.0640	-0.00447	0.02926	0.00476
x = 0.660	5.9206	0.5090	-6.3763	-1.0544	-0.00844	0.05381	0.00890
x = 0.670	5.9246	0.5099	-6.3468	-1.0528	-0.00909	0.05768	0.00957
x = 0.678	5.9279	0.5106	-6.3228	-1.0515	-0.00961	0.06073	0.01010

So for a variety of material compositions used in Mid -IR QCL Lasers, the estimated conduction band offset is shown in table 3.5 as compared to model solid theory results from other groups.

$$E_c^{abs} = E_{v,avg}^{abs} + \frac{\Delta_0}{3} + \Delta E_v + E_g(\Gamma) + \Delta E_c \tag{3.28}$$

Material	Δ_{Ec} (Calculated)	Δ_{Ec} (Quoted)
$In_{0.600}Ga_{0.400}As/In_{0.365}Al_{0.635}As$ [2]	0.722	0.690
$In_{0.600}Ga_{0.400}As/In_{0.440}Al_{0.560}As$ [24][25]	0.61917	0.620
$In_{0.660}Ga_{0.340}As/In_{0.346}Al_{0.654}As$ [26]	0.76204	0.825
$In_{0.670}Ga_{0.330}As/In_{0.362}Al_{0.638}As$ [3]	0.74189	0.800
$In_{0.678}Ga_{0.322}As/In_{0.365}Al_{0.635}As$ [27][28]	0.73969	0.730
$In_{0.670}Ga_{0.400}As/In_{0.300}Al_{0.700}As$	0.82812	—

Table 3.5: Various Conduction Band Offsets - Quoted values from papers, Calculated values from Model Solid Theory

Table 3.6: Simulation Parameters [3]

	m_c^*	E_g (eV)
$In_{0.670}Ga_{0.330}As$	0.04022	0.572
$In_{0.362}Al_{0.638}As$	0.09337	2.0061
ΔE_c (eV)	0.78	

The values computed here should be taken as a starting point for our simulations and band structures due to the large amount of uncertainty because of the effects of strain. Hopefully these parameters can be refined through various measurements.

3.2 Monte Carlo Simulations Results

Two structures were simulated with the Monte Carlo code. The first was the Injectorless Structure from [2]; the second was the miniband structure from Razeghi with the highest wall plug efficiency so far [3]. These two structures were chosen mainly due validate the effectiveness of Monte Carlo simulations for predicative value.

3.2.1 07-606 MIT LL - Razeghi Design

Figure 3-3 shows the Monte Carlo simulation results at 300 K in comparison with measured IV curves from devices grown and fabricated by Lincoln Labs. Unfortunately, only a few selected data points were considered valid for electron transport. In the Monte Carlo simulations scattering and transport are determined by the form factors due to the wavefunctions. Unfortunately, this means the simulation is very sensitive to anticrossings. States that delocalize and

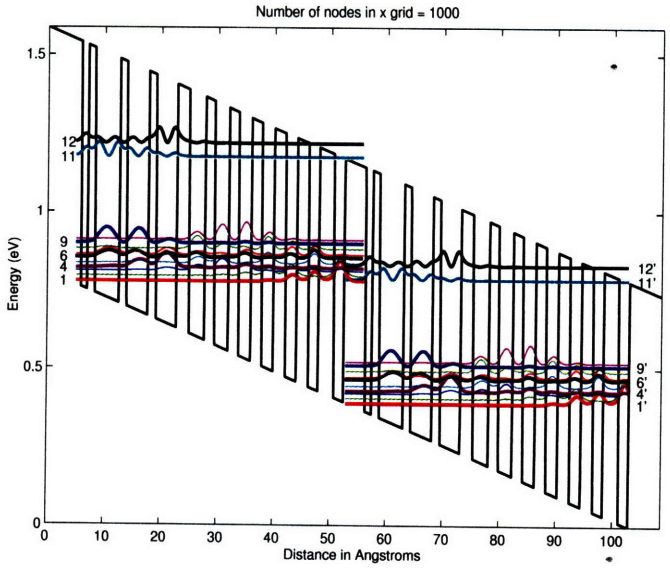

Figure 3-2: Two Module Bandstructure of Miniband QCL structure from Razeghi 4.7 μm [3]

extend across an entire module results in overestimated currents causing large current spikes in the simulated IV. Over all the simulated IV curve agrees with experiment about the turn on voltage, but differs for the series resistance. Overall, it appears that the Monte Carlo simulation is overestimating the current, which may be a sign that coherent transport might not be entirely valid for transport simulations. However, there is a possibility that parasitic voltage drops might be the cause for the discrepancy between the two curves. Figure 3-4 shows the simulated IV including all bias points. The presented IV curve in figure 3-3 is manually filtered to remove these spurious bias points where anticrossings occur. The spurious anticrossings can be removed by looking at the anticrossings strengths between two states. The general rule of thumb has been to eliminate anticrossing points if the strength of the anticrossing between two states is less than 1 or 2 meV. For the miniband design, there are a large number of states and anticrossings that occur in the miniband. For this design, the issues of anticrossing are primarily between levels (1) to (9) anticrossing with levels (11) and (12). Figure 3-5 shows one such example of how a state can be spatially delocalized and actually span an entire module.

Furthermore, all the simulations yield a definitive negative differential resistance (NDR) mode, where after the peak designed current point, the current starts to fall off as the levels move out of alignment. However experimentally, parasitic channels or tunneling into the continuum, which are not included in our simulations, usually prevent the observation of NDR. Besides IV,

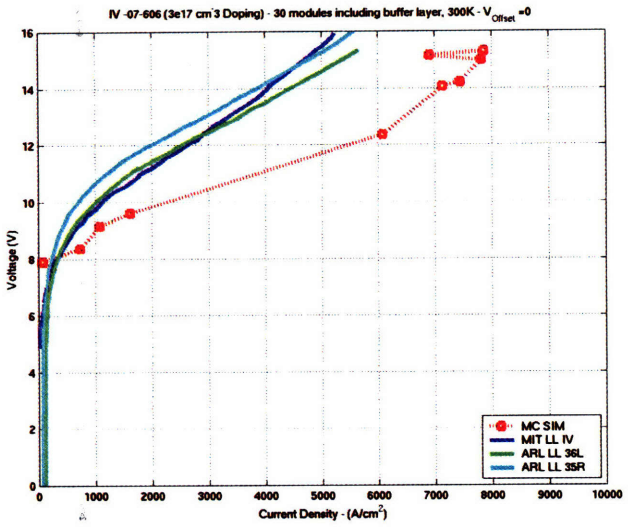

Figure 3-3: Monte Carlo simulated IV versus experimental IV

another parameter we can extract is the gain at various bias points.However, similar to the IV curve specific points must be chosen to attempt to eliminate spurious solutions. The gain versus current density curve in Figure 3-6 is computed given the steady state populations of the system using equation 2.69. From this curve we can estimate the Gain versus Current slope as well as peak gain current at $\approx 6000 A/cm^2$, with a slope of 2.5 $\frac{1/cm}{kA/cm^2}$, without taking into account modal overlap. These gain calculations assume a linewidth of 25 meV.

Figure 3-7 shows the subband populations settling in time. All the electrons are initially assumed to be evenly distributed among the subbands. The simulation for the peak gain does show a clear population inversion; however, it is obvious that it is difficult to interpret the mechanisms controlling scattering into and out of 12 different bands.

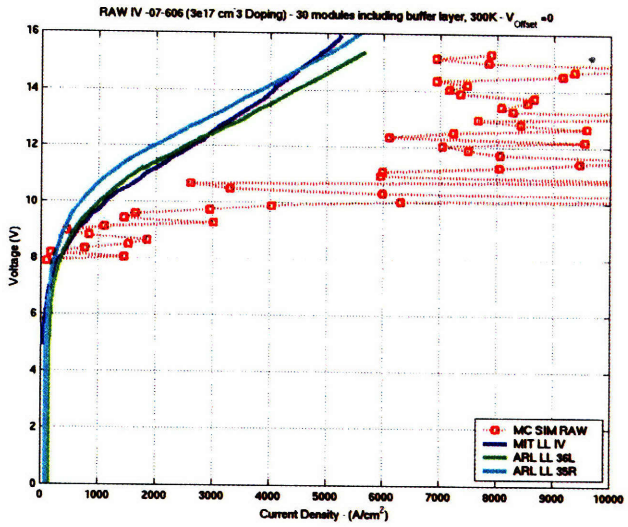

Figure 3-4: Raw simulated IV curve

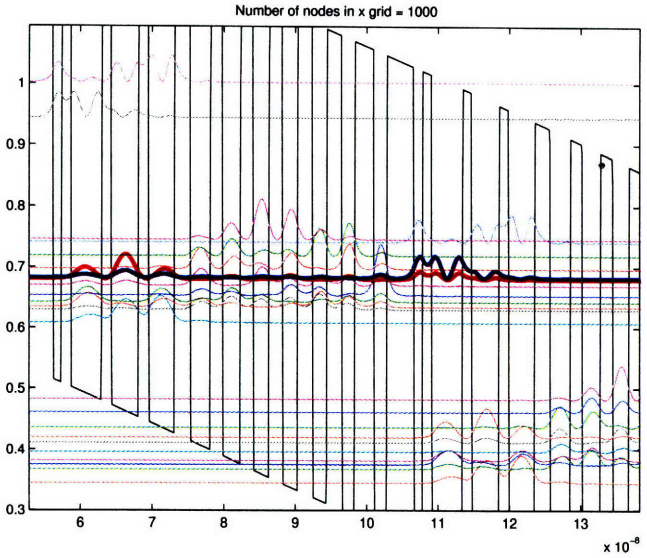

Figure 3-5: Example of Anticrossed state.

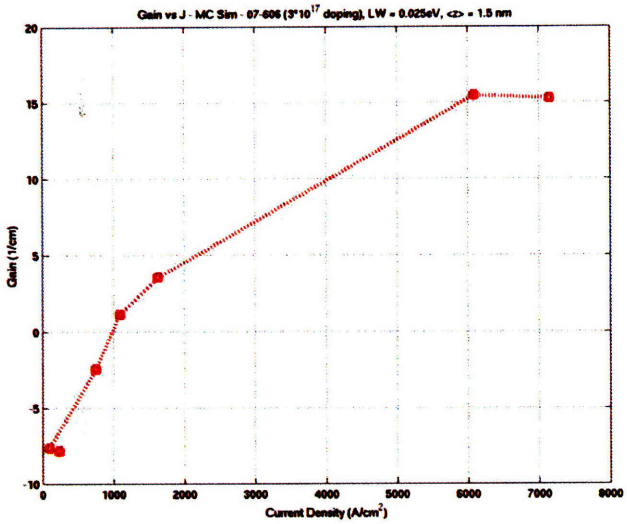

Figure 3-6: Gain versus Current Density for MIT 606 Series

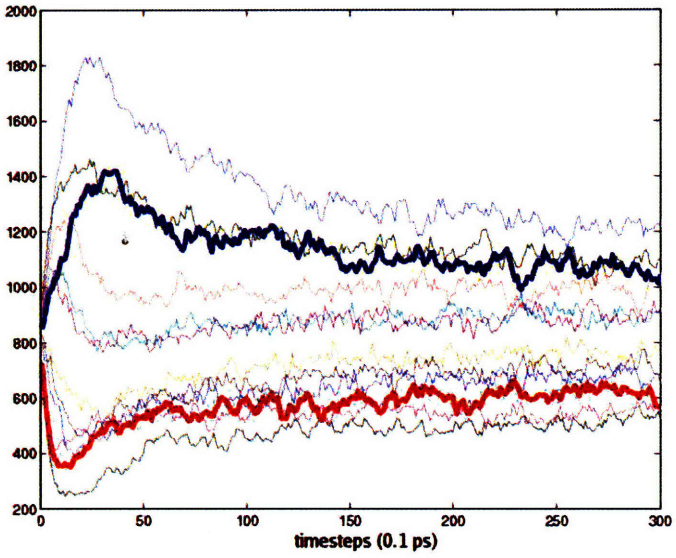

Figure 3-7: Subband Populations versus Simulation Time. Blue = Upper Lasing Level, Red = Lower Lasing Level

3.2.2 Injectorless 6.7 um

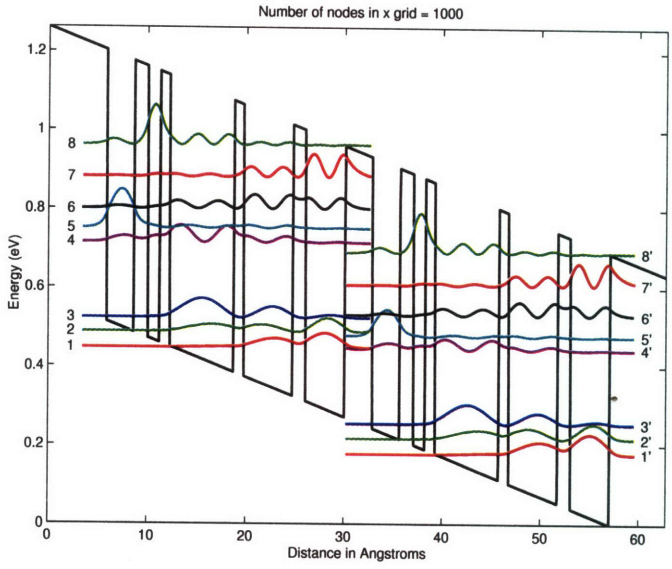

Figure 3-8: Band Diagram of Two Phonon Injectorless Design [2]

Due to the complexity of tracking 12 subbands, a simpler design was chosen for simulation. The injectorless design seemed like a promising candidate, not only for its possibility of higher WPE, but also for its simplicity. Only 5 levels play a major role in transport with 3 parasitic channels. With fewer levels the chances of a spurious anticrossing are reduced and electron transport can be tracked more readily.

Table 3.7: Simulation Parameters Injectorless 6.7 μm [2]

	m_c^*	E_g (eV)
$In_{0.600}Ga_{0.400}As$	0.04022	0.7780
$In_{0.365}Al_{0.635}As$	0.09338	1.969
ΔE_c (eV)	0.690	

In Figure 3-8 levels (1),(2),(3) are the standard LO phonon depopulation levels separated by $\approx$ 34 meV. Levels (4) and (5) are also designed to be one LO phonon apart to serve as a dual mechanism for transport across the barrier. Electrons that tunnel from 2-5' then should very quickly relax down into level (4). Levels (6),(7),(8) are assumed to be possible parasitic scattering channels; however, the anticrossings into these levels are usually $<$ 1 meV. As with

most of these simulation parameters, we have adjusted them to better match cited papers for energy separations and emission wavelength. In figure 3-9 we show the simulated IV curves from

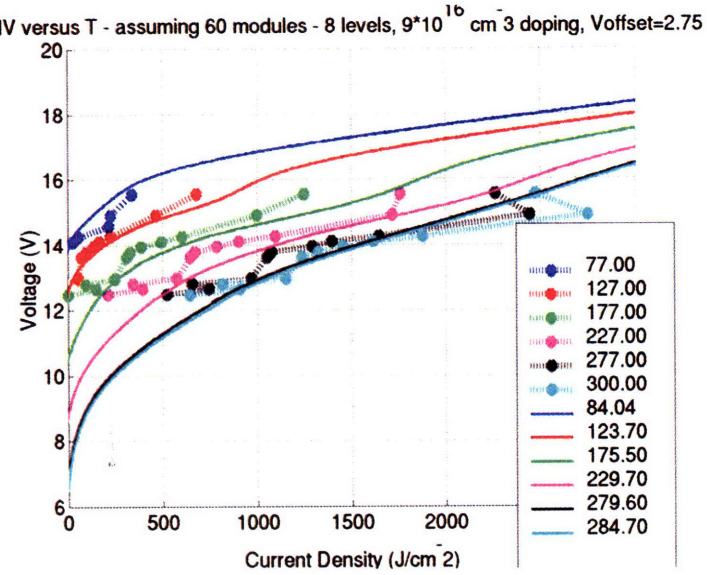

Figure 3-9: Monte Carlo Simulated IV versus Temperature compared to Experimental Data

the Monte Carlo simulations versus temperature. A sample from the WSI [2] was measured by Qi Qin for the temperature and output response, which is overlayed with the simulated IV in figure 3-9. For the purpose of better matching, we assumed a fixed voltage offset of 2.75 V, which we believe could be due to a possible parasitic voltage drop. Furthermore, no documentation seems to exist for the exact doping of the structure, we assumed a doping from [2]; however, it is possible that the doping might have been slightly higher or lower. The IV curves given here have also been selectively filtered for spurious anticrossings.

Due to the reduced number of levels, more simulations could be run within a reasonable time, allowing us to simulate the structure versus temperature. With the inclusion of the voltage offset, the simulated IV curves appear to agree pretty well with the experimentally measured ones in terms of temperature behavior. Furthermore, from the population inversions and gain, we can extract the gain-current relation. If we define a level for the waveguide loss, we can then define a threshold current by the intersection of the gain versus current and the fixed waveguide loss.

An unique feature of the injectorless design has been its ability to report some of the lowest threshold current densities at 77K. This low current threshold implies that once a small amount of current begins to flow, it almost immediately achieves lasing, which is indeed the

case from our simulations in figure 3-10. In fact one can see in figure 3-11 that the threshold current density increases exponentially as the temperature is increased from 77K up to 300K.

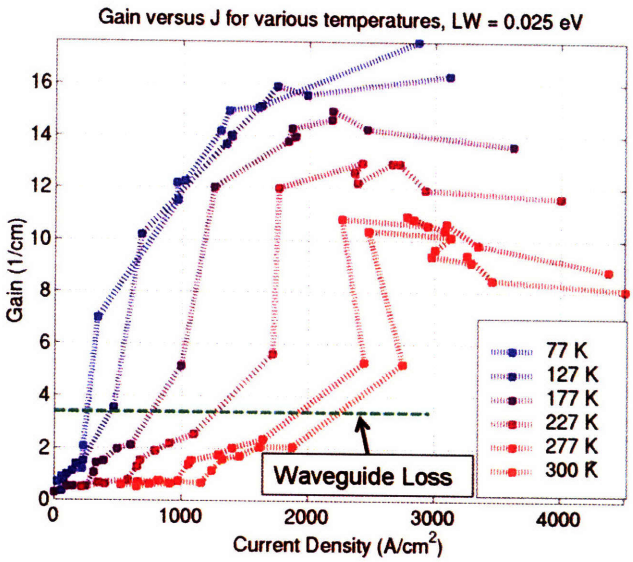

Figure 3-10: Injectorless Gain versus Current Density for various temperatures

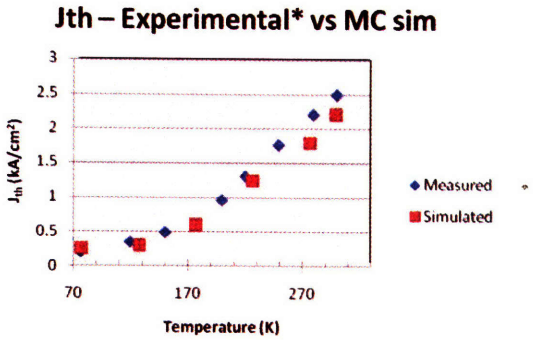

Figure 3-11: Current Density Threshold for Injectorless Design

With our defined waveguide loss, we can see that the simulated threshold current density and the experimentally measured current densities agree pretty well. This suggests that for these simplier structures Monte Carlo Simulations may be more accurate and useful for optimizing these designs. Returning to the original question of what causes this exponential increase in threshold current density, we can track the upper and lower lasing subband levels across various temperatures and bias. Figure 3-12 provides a useful example of how Monte Carlo simulations

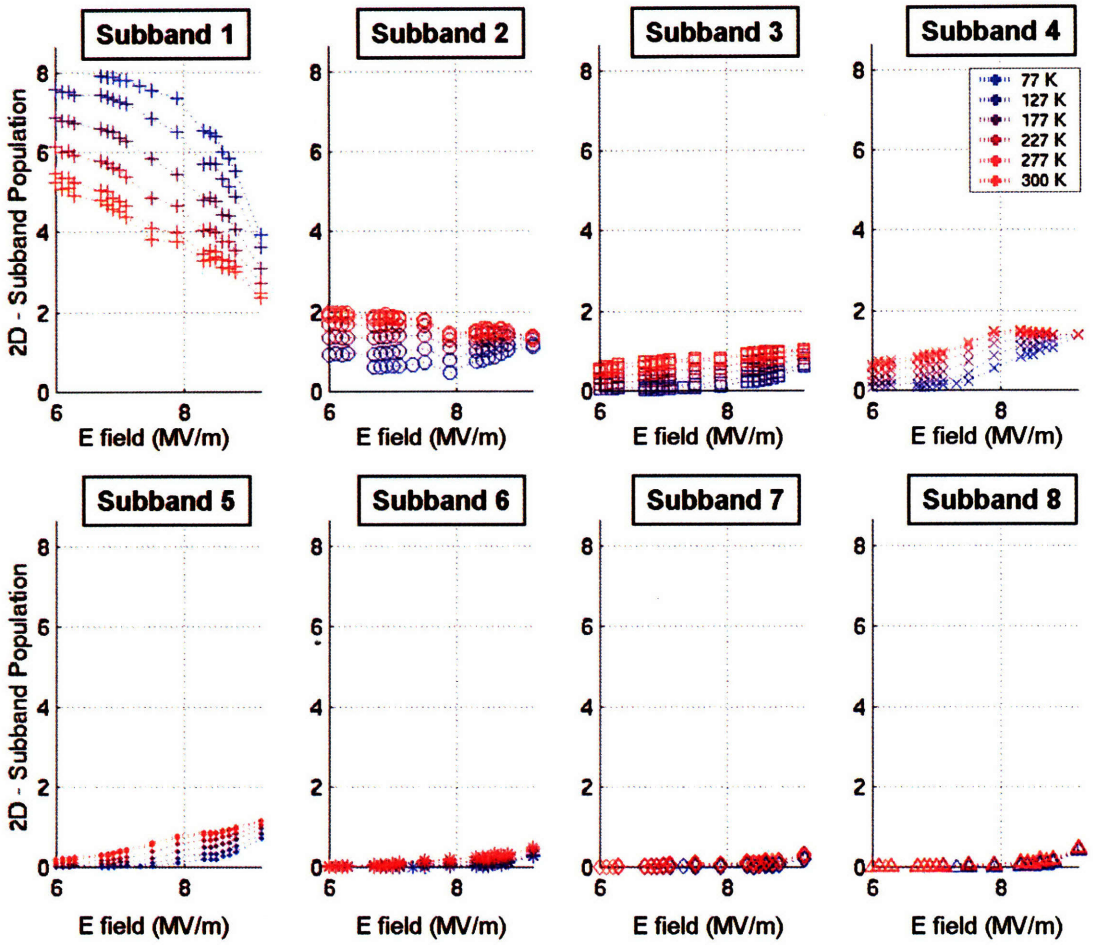

Figure 3-12: Current Density Threshold for Injectorless Design

can provide information about how the populations are affected by temperature. It appears that levels (6),(7),(8) do not contribute a significant amount to electron transport at threshold and at low temperature. Furthermore, it becomes more clear that the decrease in gain with respect to temperature is due to a fast rise in (3) compared to level (4). This might signal that thermal backfilling might be something to seriously consider in the performance of injectorless devices at higher temperatures. This can be achieved through changing the thickness of the injector barrier to help facilitate resonant tunneling into the next module. These design points will be of importance in influencing some of our own injectorless structures.

Chapter 4

Experimental Setup

In order to measure and characterize QCL devices a measuring and testing platform had to be constructed. The main attributes required a temperature controlled measuring platform as well as an automatic computer controlled software. We also required pulsed and continuous wave (CW) Light-Current-Voltage (LIV) measurements. Unfortunately, for Quantum Cascade Lasers the current and voltages are much higher than normal laser diode drivers.

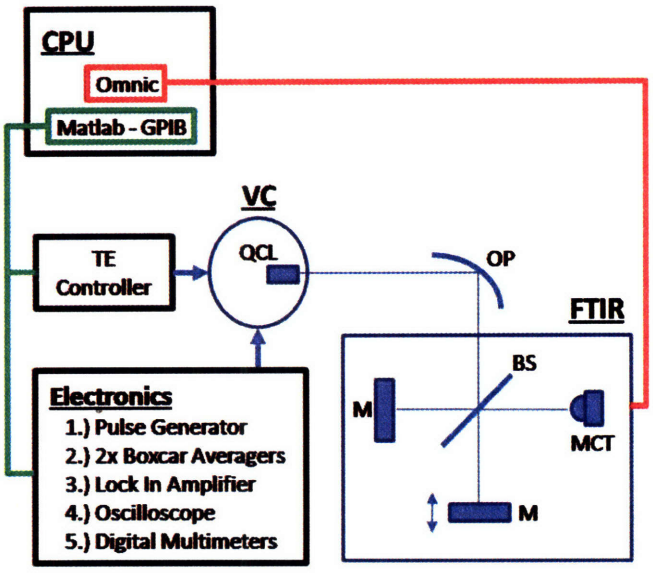

Figure 4-1: Experimental Setup

4.1 Electronics

Figure 4-1 shows the basic configuration for our setup. In order to bias our devices we purchased an Avtech 1011-b pulse generator which can provide pulse widths between 100ns - 1μs with 10 % duty cycle and current pulses upto 2-4 A with use of a transformer. Furthermore, we also purchased a ThermoFisher Nicolet 8700 FTIR spectrometer for measuring laser spectra and electro-luminescence. The FTIR is equipped with a Liquid Nitrogen cooled Mercury-Cadmium-Telleride Detector. Most of the electronics for measuring and biasing the device were available commercially. However, a custom vacuum chamber, Thermoelectric Cooler stage, as well as, software were still required.

4.2 MATLAB GPIB software

To automate the data collection process we chose the General Purpose Interface Board (GPIB) standard on most electronic devices. This is a standard protocol to interface with most pieces of scientific equipment. Traditionally, most implementations are done using LabView software due to its ease with graphically programming; however, we found it easier to implement the device control through the instrument control toolbox in MATLAB. This was mostly due to the easy integration of plotting and math functions as well as their easy to use GUI software GUIDE for constructing custom interfaces. Moreover, MATLAB provides a more conventional programming environment than LabView, which makes software maintenance easier. Figures 4-2 and 4-3 are examples of the interface screen. The only device that did not have GPIB control was the TE Cooler Temperature controller, which had its own serial port commands. The MATLAB interface includes control over all components including setting the PID controller and settings on the TEC cooler. This allows one to perform temperature dependent measurements on devices.

4.3 Vacuum Chamber - TEC Cooler

In order to test the temperature performance of our devices, a Thermoelectric cooling stage had to be implemented. A Thermoelectric Cooler from Ferrotec was purchased due to compatibility with a serial port controlled PID temperature controller. A custom rack also was constructed

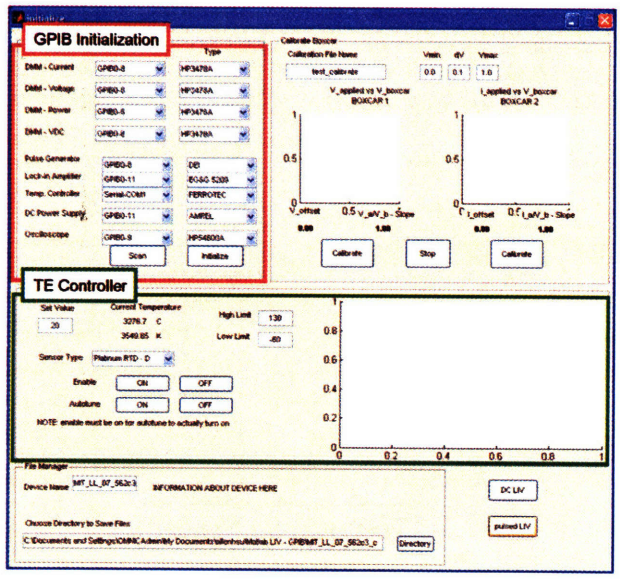

Figure 4-2: MATLAB GPIB Initialize Devices

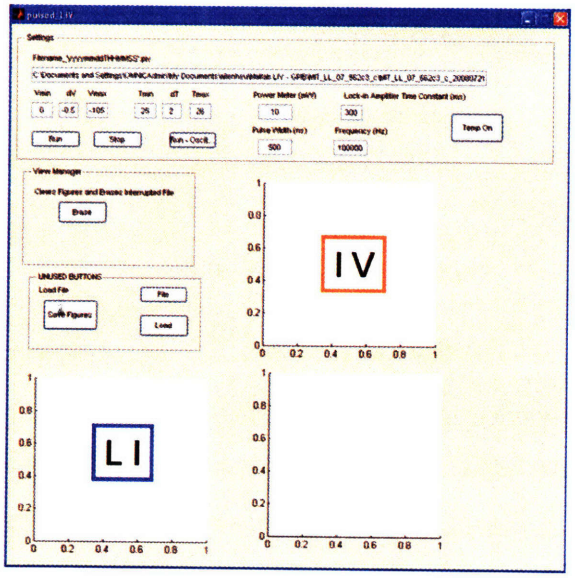

Figure 4-3: MATLAB GPIB pulsed LIV Screen

to house the temperature controller and DV voltage power supply for the TEC. The operating temperature ranges for this TE cooler were designed to go from -40 to 100 Celsius. Due to issues of ice and condensation, the TEC cooler stage had to be housed in a Vacuum Chamber that could be pumped down to remove any water vapor. The entire Vacuum Chamber Setup consisted of a QCL mount, Vacuum Chamber, and TE Cooler stage.

4.3.1 QCL Mount

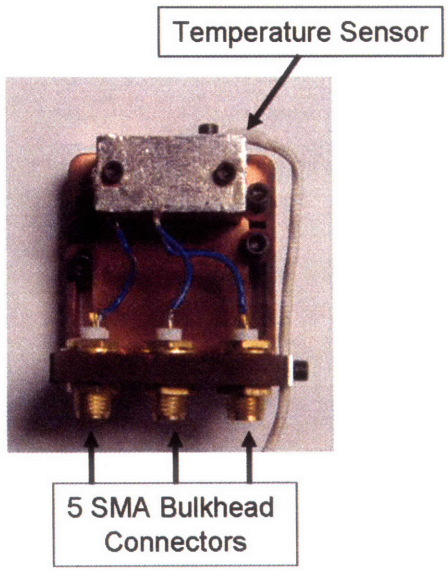

Figure 4-4: QCL Mount

The copper mount for this device included 5 Bulkhead SMA connectors, designed for eventually parallel testing of QCL devices. Furthermore, the TE cooler stage requires the need for a Temperature Sensor for its feedback PID Controller. A Platinum Resistance Temperature Detector (Pt RTD) from Omega was purchased which was precalibrated with the PID feedback controller. The sensor had to be thermal epoxied onto a metal plate, which was then screwed onto the front of the mount. To ensure good thermal contact with the QCL and with the TEC stage, indium foil was used.

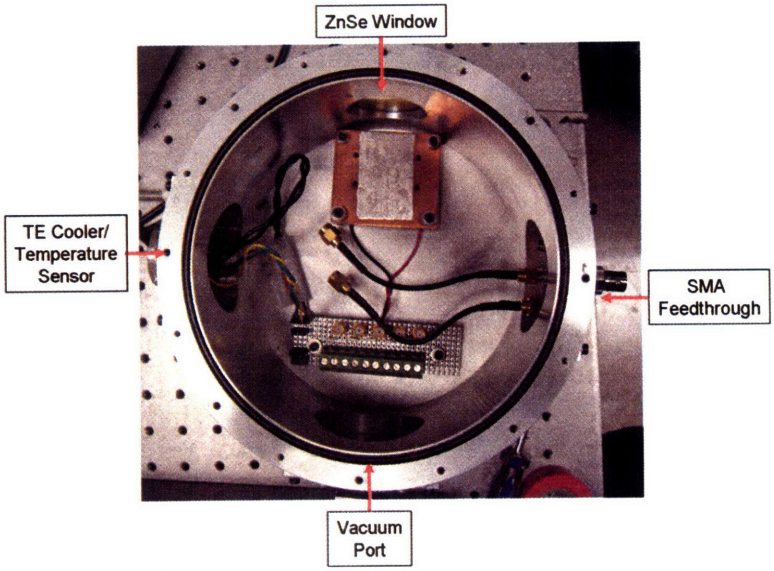

Figure 4-5: Vacuum Chamber from the Top

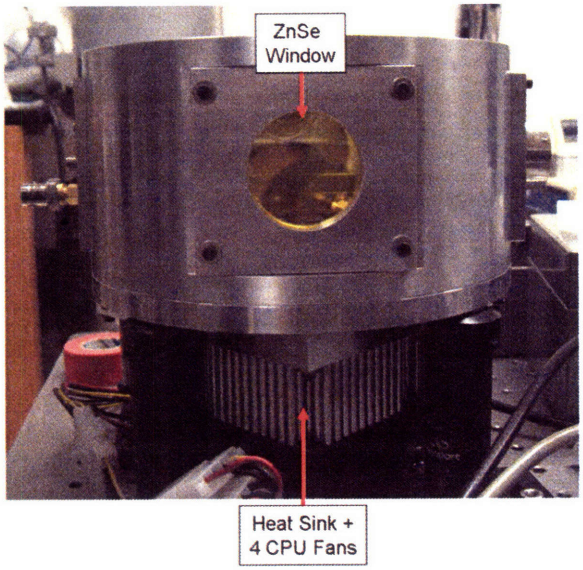

Figure 4-6: Front View of the Vacuum Chamber

4.3.2 Vacuum Chamber

The Vacuum chamber as seen from figure 4-5 is a standard cylindrical chamber with O-Ring groves to provide air tight sealing upon compression. The vacuum chamber was designed with 3 modular side wall flanges that can be customized if necessary and a window flange. The window material chosen was a Zinc Selenide window flat from ISP optics. ZnSe was chosen due to its transparency in the visible as well as its resistance to humidity. The ZnSe window has a transparency of ≈ 95 % accross 3-12 μm. The three other side flanges include a electronics output hole designed for connecting the TE cooler and temperature sensor. For improved pulsed shape performance, we also used 5 bulkhead hermetically sealed mounts with custom SMA coaxial cables for connecting to our QCL Mount. The final flange was a vacuum valve for sealing and opening the chamber during its pump down process. Internally, there is an electronics buffer board for providing a point of contact between the temperature sensor on the Mount and the electronics port with the TEC cooler.

Figure 4-6 shows a better view of the ZnSe window. Furthermore, the bottom of the VAC chamber has a large area pin fin heat sink purchased from Cool Innovations. In addition, to improve the heat sinking efficiency of the bottom side, 4 standard CPU fans were attached and powered by a wall plug power supply. The heat sinking on the bottom side was necessary since the TE cooler purchased provides a temperature differential between its hot and cold side given a specific heat load. The TE Cooler purchased from Ferrotec provides $\Delta T = 70$ assuming no heat load. Therefore, in order to obtain the lowest temperature performance the heat sink helps dissipate excess heat to maintain room temperature on the hot side.

4.3.3 Thermoelectric Cooler and Temperature Controller

For our Thermoelectric cooler, we utilized a 2 stage TE cooler purchased from Ferrotec, which has a reported $\Delta T \approx 70$ for no load. This has yielded for us in our Vacuum Chamber a lowest temperature of -43 deg C, after a time of 36 minutes, with a pressure of 8.4e-5 mbar. In order to achieve good thermal contact between the TE stage and the hot and cold plate, a variety of methods were explored. This included both attempts with indium foil and Artic Silver 5 High-Density, Polysynthetic silver thermal compound for mounting and compressing the TE cooler stage. For the large heatsink on the backside, Adhesive Interface pads using aluminum oxide

pads were needed for large surface thermal contact. Through a variety of methods, thermal grease seemed to provide the best performance. The indium foil, was not as good at filling airgaps between the top ceramic contact of the TE cooler as compared to the thermal grease. However, the indium foil was still used between the QCL mount and the hotplate for disassembly reasons.

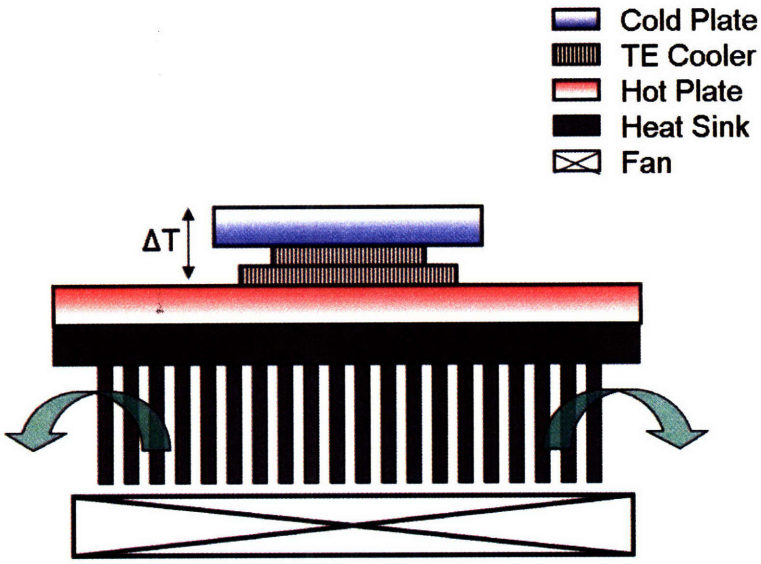

Figure 4-7: TEC Cooler Setup

Chapter 5

Designs

5.0.4 MIT 07-674 - Injectorless 1

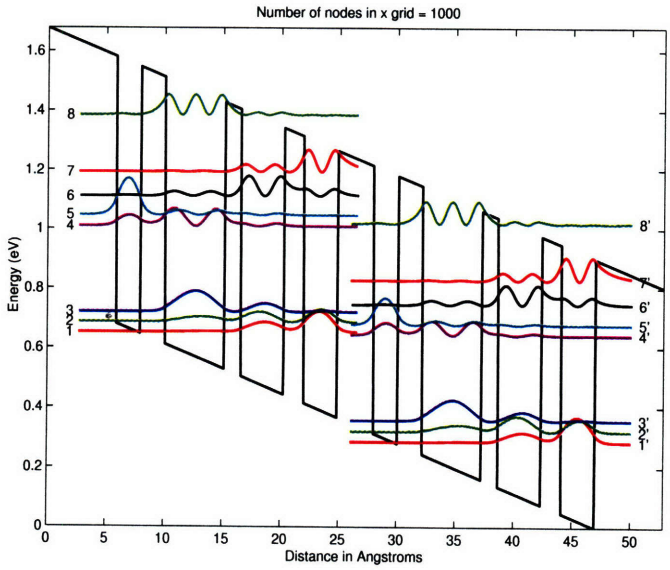

Figure 5-1: Band Diagram of MIT 674 Injectorless Design - Two Modules - Layer Thickness (Å) **21/21**/51/14/37/17/29/**32**. Layers start with a well and bold layers are doped $9 \times 10^{16} cm^{-3}$. Material Composition: $In_{0.66}Ga_{0.34}As$/ $In_{0.30}Al_{0.70}As$. Designed Bias is 158 kV/cm.

Here we present our first design for a modified injectorless design. The basic structure is similar to previous injectorless designs with the modification of simplifying it further to 4 wells. This was done to reduce any parasitic subbands and to further reduce passive layers into the active region that could contribute to optical loss. The upper lasing level is level (4) and the lower lasing level is (3). As seen from table 5.1, the energy spacing between levels (3),(2),(1) are

Table 5.1: Energy Spacing

Δ E (meV)	1	2	3	4
2	**33.69**			
3	67.31	**33.62**		
4	349.75	316.05	**282.43**	
5	383.53	349.84	316.22	**33.79**

Table 5.2: LO phonon scattering times. $\tau_{lifetimes} = \sum 1/\tau_i$

τ (ps) (300K)	1	2	3	4	$\tau_{lifetime}$
2	0.24				0.24
3	1.62	0.23			**0,20**
4	22.89	6.46	3.53		**2.08**
5	26.14	10.84	7.04	0.18	0.17

Table 5.3: Dipole Moment

$\langle z \rangle$ (nm)	1	2	3	4
2	2.49			
3	0.07	2.67		
4	0.05	0.34	**1.03**	
5	0.01	0.22	0.85	2.67

Table 5.4: Simulation Parameters

	m_c^*	E_g (eV)
$In_{0.66}Ga_{0.34}As$	0.039	0.625
$In_{0.30}Al_{0.70}As$	0.100	2.222
ΔE_c (eV)	0.89	

Table 5.5: Anticrossings Strengths

	Δ_0 (meV)	@ Bias (kV/cm)	$J_{max}(kA/cm^2)$
2-5"	5.61	158	19.19
1-4"	4.94	158	2.62

chosen to be one LO phonon apart, which at 300 K corresponds to lifetimes for level (3) of $\approx$ 0.20 ps. This corresponds to a voltage defect of 67.31 meV. The levels (5) and (4) are also one LO phonon apart for parallel depopulation out of the module. Furthermore, with our design we wanted to further increase the upper state lifetime by attempting a slightly more diagonal transition which is evident from the reduced dipole moment 1.03 nm, but the longer upperstate lifetime of 2.08 ps. This diagonal transition has added benefits for overall upperstate lifetime due to reduced tunneling into the continuum.

To achieve the diagnolity as well as the LO phonon resonance of (5) and (4), we designed levels (5) and (4) to anticross slightly to pull the wavefunction further over to the left as well as maintain the energy separation across biases. The added benefit of this diagnolity is the increased coupling between states from the previous modules for resonant tunneling.

To assess the strength of anticrossing, we simulate three modules and compute the minimum energy separation between states. Using the naming convention where the left module is X", center module as X, and right module as X', we show the anticrossing strengths in figure 5-2 and the computed current density using equation (2.94). Another concern with the design was parasitic channels that could allow electrons to be lost to the continuum. Figure 5-3 and table 5.6 focus on the anticrossing into a high level bound state. Using the expression for J_{max} we can also estimate the amount of time it takes to resonantly tunnel given an anticrossing strength. We assumed a worse case scenario of 1 ps lifetime for level 8, due to the strong coupling spatial overlaps with states in that well. We attempted to keep these parasitic channels below 0.5 meV, which generates resonant tunneling on the order of 10's to 100's of picoseconds, which is much longer than the normal scattering processes inside the QCL module. To control these parasitic channels we had to thicken the injection barrier slightly to 32 Å.

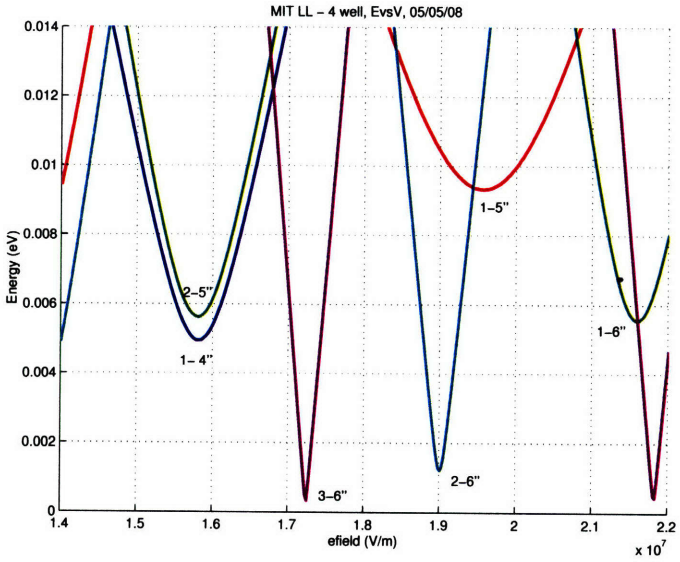

Figure 5-2: Anticrossings Strengths

Table 5.6: Parasitic Anticrossings Strengths - $\tau_{lifetime} = 1ps, \tau_{||} = 100fs$

	Δ_0 (meV)	@ Bias (kV/cm)	$\tau_{eff}(ps)$
1'-8"	0.14	164	444.08
2'-8"	0.23	156	165.80
3'-8"	0.10	148	868.49
4 -8"	0.34	169	76.96
5 -8"	0.33	154	81.57

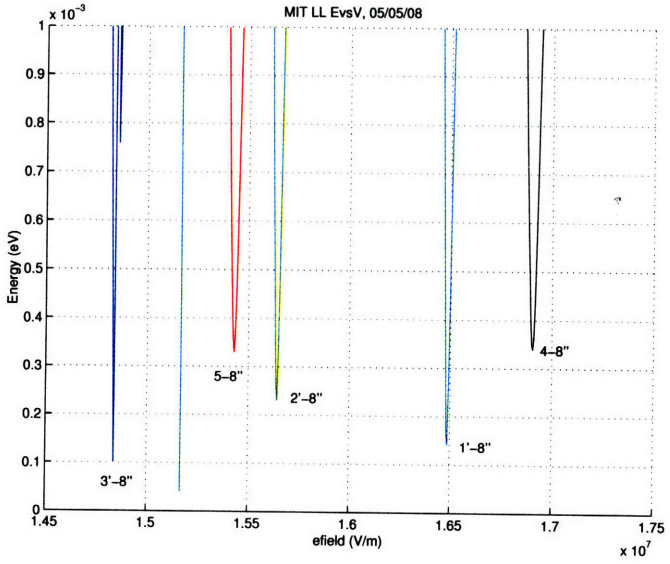

Figure 5-3: Parasitic Anticrossing Strengths

5.0.5 MIT LL Injectorless 2

We also designed a slightly modified structure based upon the same 4 well system, except at a longer wavelength of 4.8 μm and with states (3),(2),(1) designed to be spaced apart slightly larger than one LO phonon. We have also included all the necessary design files. There were some slight issues with parasitic channels of level (8). This is because since we went to a longer wavelength, level (8) now becomes closer to resonance at the design bias. This has caused the anticrossing strengths for this design to be slightly higher than previously.

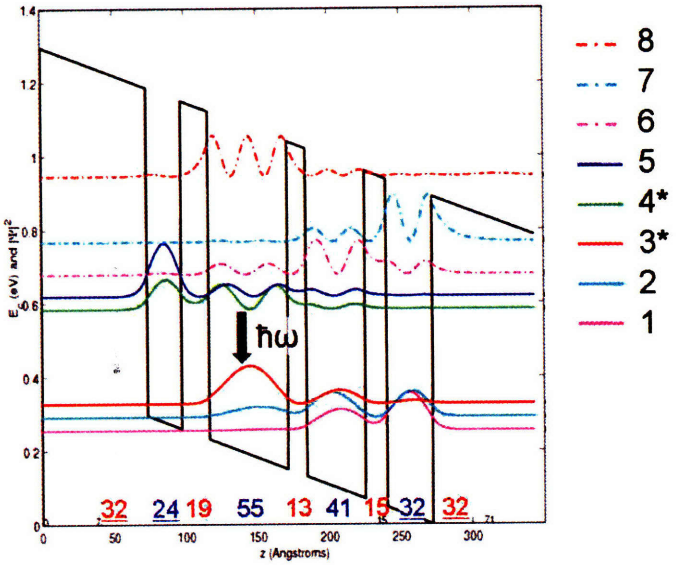

Figure 5-4: Band Diagram of MIT LL Injectorless Design 2 - Two Modules - Layer Thickness (Å) **32**/**24**/19/55/13/41/15/**32**. Layers start with a well and bold layers are doped $2 \times 10^{17} cm^{-3}$. Material Composition: $In_{0.65}Ga_{0.35}As$/ $In_{0.30}Al_{0.70}As$. Designed Bias is 148 kV/cm.

Table 5.7: Energy Spacing

Δ E (meV)	1	2	3	4
2	**37.64**			
3	72.53	**34.89**		
4	330.2	292.5	**257.6**	
5	365.2	327.5	292.6	**35.02**

Table 5.8: LO phonon scattering times. $\tau_{lifetimes} = \sum 1/\tau_i$

τ (ps) (300K)	1	2	3	4	$\tau_{lifetime}$
2	0.30				0.30
3	2.10	0.30			**0.26**
4	20.3	6.87	3.04		**1.91**
5	19.3	10.87	6.89	0.22	0.21

Table 5.9: Dipole Moment

$\langle z \rangle$ (nm)	1	2	3	4
2	2.41			
3	0.05	2.44		
4	0.01	0.25	**1.15**	
5	0.06	0.10	0.94	2.91

Table 5.10: Simulation Parameters

	m_c^*	E_g (eV)
$In_{0.66}Ga_{0.34}As$	0.040	0.660
$In_{0.30}Al_{0.70}As$	0.100	2.222
ΔE_c (eV)	0.89	

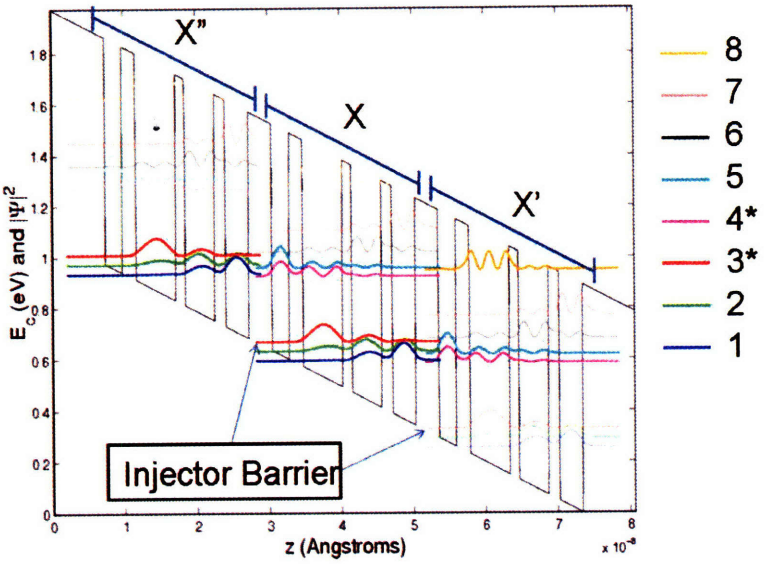

Figure 5-5: Parasitic Anticrossing Strengths

Table 5.11: Anticrossings Strengths

	Δ_0 (meV)	@ Bias (kV/cm)	$J_{max}(kA/cm^2)$
2-5'	4.44	138	32.762
1-4'	4.75	140	6.702

Table 5.12: Parasitic Anticrossings Strengths - $\tau_{lifetime} = 1ps, \tau_{||} = 100fs$

	Δ_0 (meV)	@ Bias (kV/cm)	$\tau_{eff}(ps)$
1'-8"	0.13	149.9	514.713
2'-8"	0.45	142.4	44.79
3'-8"	0.27	133.4	120.86
4 -8"	0.25	154.2	140.64
5 -8"	0.30	140.2	98.28

5.1 Strain-Balancing

With a shorter active region, a larger voltage bias must be applied to generate the appropriate electric field strength. This requires a large degree of electron confinement; normally this is accomplished through strained structures, which change the conduction band offsets due to deformation potentials. In our designs, for the shorter wavelength, we opted for a 1.5 percent strain barrier with an estimated conduction band offset of about 0.89 eV upon discussion with Joe Donnelly and our collaborators at Lincoln Labs, which is close to out estimate from Model Solid Theory.

When thin layers of material are grown on a substrate, the epitaxial layer's lattice constant matches the in plane substrate lattice constant. This either compresses or expands the in plane lattice constant, which due to Poisson's ratio, imparts also a change in the perpendicular lattice constant. As this epitaxial layer grows thicker and thicker, eventually far away from the interface the material will naturally relax back to its unstrained form. When this relaxation occurs, this relaxation causes various defects all which decrease the quality of the interface. This is a critical issue especially for Quantum Cascade Lasers, where electron transport through barriers and linewidth of laser emission are all dependent on the interface quality. However, these defects do not occur immediately and in fact are controlled by the height of the epitaxially grown structure, which is defined as the critical layer thickness by Blakeslee, and Matthews.

$$h_c = \frac{b}{2\pi f}\frac{(1 - v\cos^2\alpha)}{(1+v)\cos\lambda}\left(ln\frac{h_c}{b} + 1\right) \tag{5.1}$$

where λ = angle between the slip direction and that direction in the fill plane which is perpendicular to the line of intersection of the slip plane and the interface, v is the Poisson ratio, b is the strength of the dislocations, f is twice the maximum value of the strain $\epsilon_max = 1/2f$. This critical layer thickness is typically on the order of 100's of Å, after which one would expect to see misfit dislocations along the interface. However, typically QCL structures are often 1-2 μm thick. Therefore, in order to grow arbitrary thicknesses of strained layers, one must use strain balancing. By balancing the strain between alternating compressive and tensile strained layers, the overall strain of the system is balanced and one can grow high quality strain interfaces.

These highly strained structures are crucial for shorter wavelength QCL structures since as the energy separation increases, the upper state level gets closer and closer to the top of the

conduction barrier, leading to shorter upper state lifetimes as electrons more easily escape into the continuum.

The condition for determining whether a structure is strain balanced can be quantified in a variety of methods: thickness weighted method, zero-stress method, etc [30]. These methods attempt to balance the stored elastic energy due to compression and tension. However even with complex methods, most QCL structures achieve strain balancing using the simple Thickness Weighted Method.

$$t_1\epsilon_1 + t_2\epsilon_2 = 0 \tag{5.2}$$

$$\epsilon_i = \frac{a_0 - a_i}{a_i} \tag{5.3}$$

where a_0 is the substrate lattice constant, and a_i is the lattice constant of the epitaxial layers, assuming, epitaxial layers are grown on a substrate with a different lattice constant.

5.2 Growth and Fabrication

The structure was grown and fabricated by MIT Lincoln Labs using a Metal-organic vapour phase epitaxy (MOVPE) reactor or Metal-organic Chemical Vapour Deposition (MOCVD), a standard method for growing epitaxial layers of compound semiconductors for laser diodes, solar cells, etc. In table 5.13 we have included the various layers that are grown for a full QCL structure. Besides the active region, various cladding layers are introduced. The InGaAs waveguide layers provide a larger index of refraction contrast with the InP than the Active region with the InP. The effect of this is to create a more uniform mode shape over the active region and confine the mode. This confinement helps reduces waveguide losses due to absorption with the contact metal layers. The InP cladding layer is therefore very important for separating the mode away from the metal. The waveguide used is standard for most QCL layers. Simulations for waveguide loss to verify the low loss and confinement factors were done by Ben Williams.

After growth of these wafers, MIT Lincoln Labs also fabricated these lasers into laser ridges with various widths of 4 μm 8μm,14μm, 20μm. Standard micro-fabrication techniques were used as well as Inductive-Coupled-Plasma (ICP) dry-etching and chemical wet-etching were done to

generate the ridge profile.

Table 5.13: Growth Sheet

Layer	Material	Thickness(A)
1	n-InP plasmon ($9x10^{18}$)	7500
2	n-InP cladding ($1x10^{17}$)	30000
3	n-InGaAs waveguide ($3x10^{16}$)	3300
4	45 stage Active Region + Buffer	10119
5	n-InGaAs waveguide ($3x10^{16}$)	3300
6	n-InP cladding ($4x10^{18}$)	30000

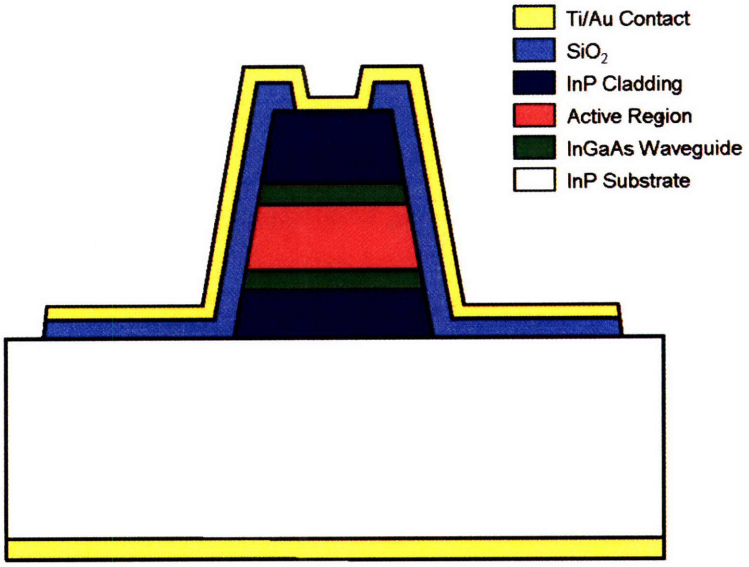

Figure 5-6: Processed Ridge Structures

5.3 Wall Plug Efficiency Metric

We estimated the efficiency of these devices assuming various parameters for waveguide loss, peak and threshold current densities, and nonradiative scattering lifetimes. Using a modified expression we can write the wall plug efficiency in terms of five main metrics. The injectorless design potentially can improve upon each of these five metrics through its simplified design.

1. Voltage Efficiency η_V - This expression is primarily optimized by minimizing the voltage defect Δ, which is the major strength of the injectorless design by nature since removing the miniband changes Δ from $\approx$ 130 meV down to 70 meV.

2. Optical Efficiency η_{opt} - since the mirror losses are fixed given a cavity length, the aim is create the lowest loss waveguide. One route is through improved fabrication to generate low loss waveguides. Another is through removing passive and possibly absorbing layers. This is the primarily motivation for using a 4 well structure in our designs. Furthermore, by reducing the number of wells, we also reduce the number of states for electrons which may help reduce absorption from bound states within the QCL module.

3. Current Efficiency η_J - the injectorless also addresses this issue through its commonly reported low threshold current densities. Measurements indicate that the injectorless designs in general at low temperature can maintain a large dynamic range, which further maximizes the current efficiency.

4. Internal Efficiency η_i - by going for a more diagonal design, we are hoping to further maximize this efficiency, due to increased τ_{32} and τ_3. Also our design assumes a conduction barrier offset of 0.89 eV, which should hopefully further reduce any thermionic emission or tunneling into the continuum from the upper state, which is critical for obtaining a higher internal efficiency.

5. Modal Uniformity η_V - This describes the modal uniformity across the active region, which for the InGaAs waveguide cladding is estimated as 95 % from [31].

$$\eta_{WP} = \left(\frac{\hbar\omega}{\hbar\omega+\Delta}\right)\left(\frac{\alpha_M}{\alpha_M+\alpha_W}\right)\left(\frac{J-J_{th}}{J}\right)\eta_i\cdot\eta_u \tag{5.4}$$

$$\eta_{WP} = \eta_V \cdot \eta_{opt} \cdot \eta_J \cdot \eta_i \cdot \eta_u \tag{5.5}$$

$$\eta_i = \frac{(\eta_{inj}\tau_3(1-\tau_2/\tau_{32})-(1-\eta_{inj})\tau_2)}{\tau_2+\tau_3(1-\tau_2/\tau_{32})} \tag{5.6}$$

Table 5.14: Wall Plug Efficiency Metric

	MIT Injectorless 1	MIT Injectorless 2
Width (cm)	0.0004	0.0004
Length (cm)	0.3	0.3
N_p	45	45
Waveguide Loss $\alpha_w(cm^{-1})$	$\approx$1	$\approx$1
Mirror Loss $\alpha_M(cm^{-1})$	2.27	2.27
Voltage Defect Δ	0.0673	0.0725
Photon Energy (eV)	0.282 (4.39 μm)	0.257 (4.82 μm)
J_{th} (A/cm^2)	$\approx$ 700	$\approx$ 700
J_{MAX} (A/cm^2)	$\approx$ 3000	$\approx$ 3000
η_{inj}	0.80	0.80
τ_2 (ps)	0.20	0.26
τ_{32} (ps)	3.53	3.04
τ_3 (ps)	2.08	1.91
η_V - voltage efficiency	0.80	0.78
η_{opt} - optical efficiency	0.69	0.69
η_J - current efficiency	0.77	0.77
η_i - internal efficiency	0.71	0.67
η_u - modal uniformity	0.95	0.95
η_{WP} - WPE	**28.9 %**	**26.4 %**

Chapter 6

Measurements

All measurements were done on samples grown and fabricated by MIT Lincoln Labs. In order to verify their growth process, they grew published designs from Razeghi [3] for benchmarking their growth process. In addition, they grew our designed Injectorless Structure with high strain. The results from the Razeghi structures have been included to verify our experimental setup and illustrate the experimental techniques used.

6.1 MIT-LL-Razeghi Design

Because our measurements were done in collaboration with MIT Lincoln Labs, we have included the measurements focused on determining the spectral properties of these lasers.

6.1.1 Electro-luminescence (EL)

For the Razeghi Devices grown, we measured EL on a series of non-lasing broad area devices. These structures were wet-etched and without any side wall coverage; however, they did not lase for some reason. The ridge widths were 45 μm and devices were cleaved to between 1 mm to 2 mm in order to allow us to bias these devices fully. Fortunately, because these devices did not lase, the measurements should provide a better estimate of the true linewidth assuming no gain narrowing.

Figures 6-1 and 6-2 show the comparison between the linewidths of two identical structures except for a change in doping. We notice that there is indeed some increase in the linewidth,

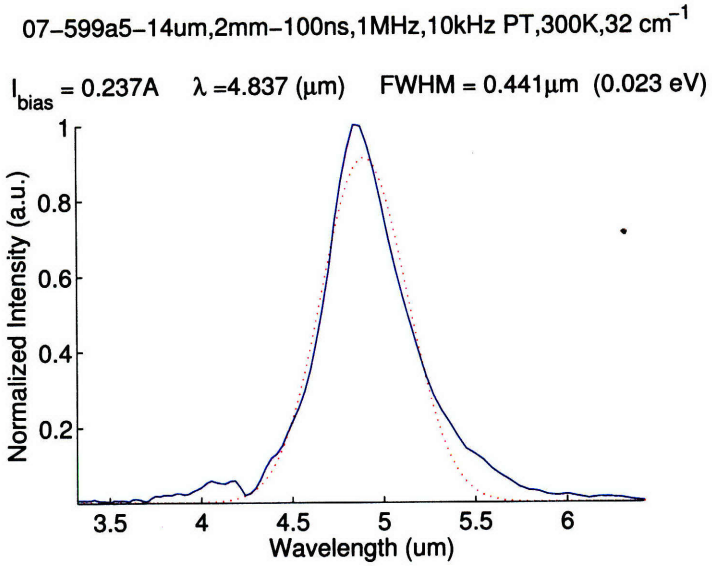

Figure 6-1: 599 EL Spectrum - Doping $1 \times 10^{17} cm^3$, FWHM = 23 meV

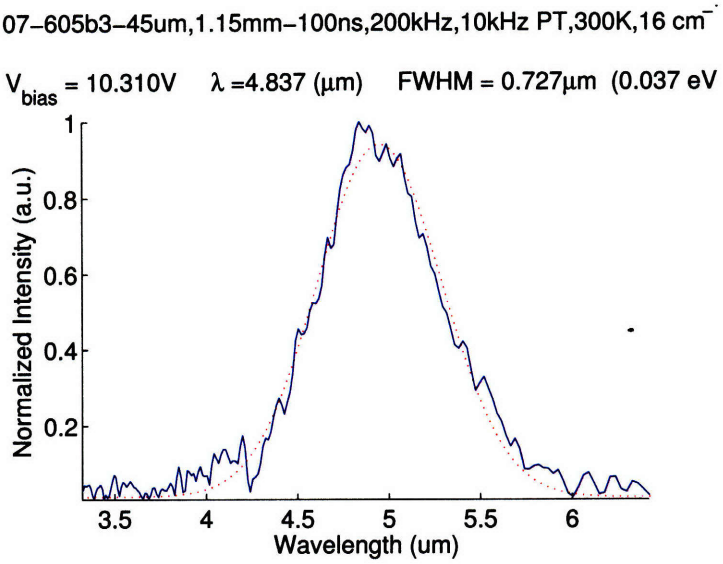

Figure 6-2: 605 EL Spectrum - Doping $2 \times 10^{17} cm^3$, FWHM = 37 meV

which may be due to doping; however, since the broad area structure was designed to be a laser there may still be some gain narrowing. In the 605 sample the linewidth varied from 0.37 meV to 0.33 with higher biases, but the gain narrowing due to lasing would generate gain narrowing of a much larger magnitude. Initially these broad area structures were fabricated and did not lase. However, the same active region was reprocessed into thin laser ridges with side wall coverage and lasing was then observed.

Furthermore, we fit the EL spectra with Gaussian fits, which seems to indicate that the broadening mechanisms are inhomogeneous line width broadening. We also confirmed that our growth and material parameters agreed with Razeghi due to close agreement between our emission wavelength and the reported designed emission wavelength from literature.

These EL measurements are also the origin of the linewidth used in our MC simulations. For our new designs we will also focus back again on obtaining EL in order to get a sense of the quality of the interfaces and the effect of pursuing a more diagonal transitions.

6.1.2 Spectrum

We also measured the pulsed spectrum at 300K at a variety of biases. Figure 6-3 shows the variations in the pulsed spectrum, which are due to a variety of transient effects. For contrast, we show the CW spectrum taken at 77K in figure 6-4, to show how the lasing spectra collapses down to one mode. These measured CW spectra will prove useful for measuring waveguide losses in these lasers.

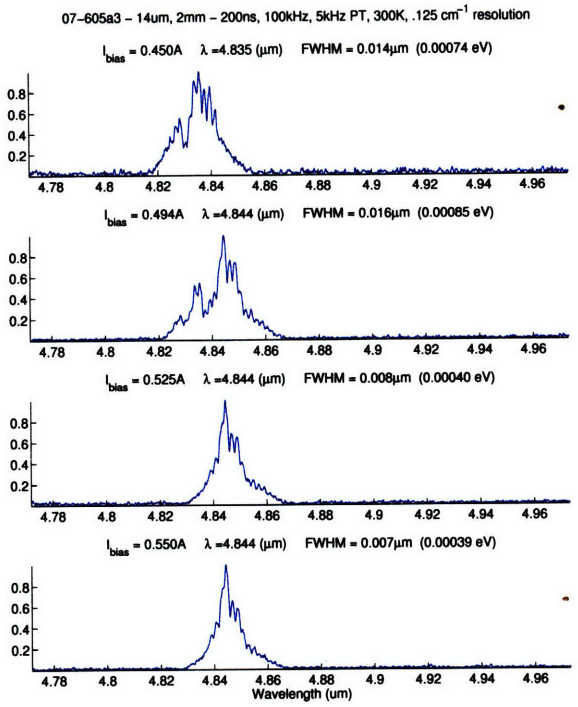

Figure 6-3: 605 Lasing Spectra - Doping $2 \times 10^{17} cm^3$

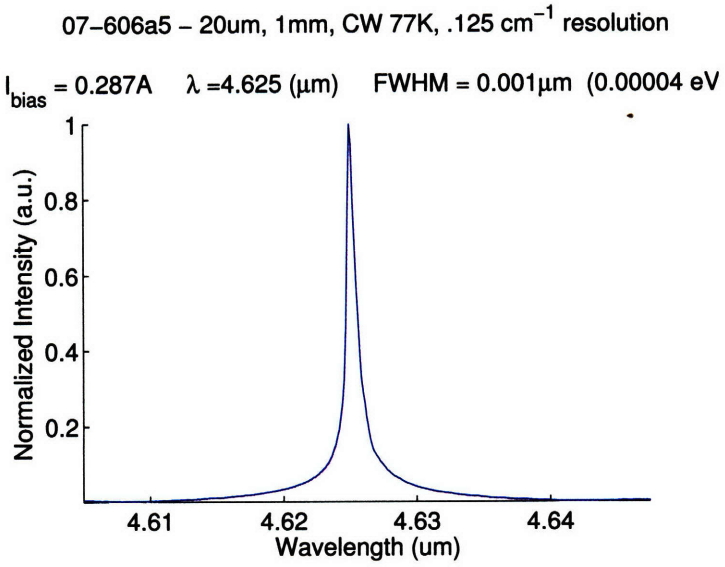

Figure 6-4: 606 CW Lasing Spectra - Doping $3 \times 10^{17} cm^3$

6.1.3 Hakki-Paoli

A key parameter for wall-plug efficiency is waveguide loss. Ideally, reducing the waveguide loss should help improve the slope efficiency. A common method for determining both gain and waveguide loss in semiconductor measurement is the Hakki Paoli method [32] [33]. As a laser's gain gets closer to threshold, Fabry Perot Fringes appear in the spectrum due to Amplified Spontaneous Emission (ASE). These fringes however can only be seen below threshold and provide information about the quality of the Fabry Perot Cavity and resonator. Traditionally, using spectral information about the contrast of the Fabry Perot Fringes, one could make inferences about the gain in the cavity and the waveguide loss as a laser reaches closer to threshold. However, due to some initial attempts, we found this method was not entirely reliable for the QCL's measured since the traditionally Hakki Paoli Method relies on only the contrast ratio, which is hard to accurately discern from spectral information and it assumes a fixed line shape function for each mode, that is difficult to fit due to shifts in index and temperature. It is also difficult to plot gain versus wavenumber using this method due to the variation from mode to mode in the spectra. Therefore, an alternative version of Hakki Paoli was developed [34][35][36]. In brief, this method through looking at the Fourier Transform of the spectral information allows one to quantify the quality of the Fabry Perot Cavity and as well quantify the gain due to current inside the cavity.

It has been shown that for a specific wavelength and a dielectric slab with two interfaces the transmission spectra is:

$$I(\beta) = \left(\frac{1-R}{R}\right)^2 \frac{b}{1+b^2-2b\cos(4\pi nL\beta)} \tag{6.1}$$

$$R = \left(\frac{n-1}{n+1}\right)^2 \tag{6.2}$$

$$b = Re^{-[\alpha - g(\beta)]L} \tag{6.3}$$

Where $\beta = 1/\lambda$, L is the length of the cavity, $\alpha - g(\beta)$ is the net gain and is wavelength dependent. However, it becomes obvious that in terms of β the transmission function is periodic since it is only relevant in the cosine term. However, we can also write this expression in terms of a Fourier Series expansion. Unfortunately, this is difficult to do directly, so we have to derive the transmission function in another common form. Let us assume we have a dielectric material,

and a normal incident beam on the dielectric slab. The reflected electric field coefficient is

$$R = \left(\frac{n-1}{n+1}\right)^2 \tag{6.4}$$

Assuming we now have an incident beam on a dielectric slab, this slab will create a resonator since light transmitted by the first interface will be reflected by the second interface and so on. We can therefore explicitly write out the strength of the electric field after all of those bounces.

$$\begin{aligned} E_t &= E_0\sqrt{1-R}e^{ikL}\sqrt{1-R}+ & (6.5)\\ & E_0\sqrt{1-R}e^{ikL}\sqrt{1-R}Re^{i2kL}+ & (6.6)\\ & E_0\sqrt{1-R}e^{ikL}\sqrt{1-R}Re^{i2kL}+Re^{i2kL}\cdots & (6.7) \end{aligned}$$

Where k describes the phase accumulated through traveling through a cavity of length L. We can include loss and net gain by assuming that our k is imaginary. Let us define a net loss term as

$$k = k_0 + i\alpha/2 \tag{6.8}$$

$$\alpha = \alpha_{waveguide} - g(\beta) \tag{6.9}$$

Where $g(\beta)$ is the net gain, assuming we might have an amplifying material. Therefore we can rewrite our expression as

$$\begin{aligned} E_t &= E_0\sqrt{1-R}e^{-\alpha L}e^{ik_0L}\sqrt{1-R}+ & (6.10)\\ & E_0\sqrt{1-R}e^{-\alpha L}e^{ik_0L}\sqrt{1-R}Re^{-2\alpha L}e^{i2k_0L}+ & (6.11)\\ & E_0\sqrt{1-R}e^{-\alpha L}e^{ik_0L}\sqrt{1-R}Re^{-2\alpha L}e^{i2k_0L}Re^{-2\alpha L}e^{i2k_0L}+\cdots & (6.12) \end{aligned}$$

Let us also define a parameter $b = Re^{-2\alpha L}$

$$E_t = E_0\frac{1-R}{\sqrt{R}}\sqrt{b}e^{ik_0L}\sum_{m=0}^{\infty}\left(be^{i2k_0L}\right)^m \tag{6.13}$$

Then in order to compute the actual intensity of the transmitted light we need to compute

$$I_t = E_t E_t^* = I_0 \frac{(1-R)^2}{R} b \sum_{p=0}^{\infty} \sum_{m=0}^{\infty} \left(be^{-i2k_0L}\right)^p \left(be^{i2k_0L}\right)^m \tag{6.14}$$

After working through the expression, term by term we can simplify the double sum

$$\sum_{p=0}^{\infty} \sum_{m=0}^{\infty} \left(be^{-i2k_0L}\right)^p \left(be^{i2k_0L}\right)^m = \left(\sum_{m=-\infty}^{\infty} \frac{b^{|m|}}{1-b^2} e^{2k_0mL}\right) \tag{6.15}$$

$$\frac{I_t}{I_0} = \frac{(1-R)^2}{R} \frac{b}{1-b^2} \sum_{m=-\infty}^{\infty} b^{|m|} e^{2k_0mL} \tag{6.16}$$

Where $k_0 = \frac{2\pi n}{\lambda} = 2\pi n\beta$, and our loss term is actually frequency dependent. Figure 6-5 shows both the periodicity as well as the amplified spontaneous emission present in the transmission function with respect to frequency.

$$I(\beta) = \frac{I_t}{I_0} = \frac{(1-R)^2}{R} \frac{b[\beta]}{1-b[\beta]^2} \sum_{m=-\infty}^{\infty} (b[\beta])^{|m|} e^{4\pi n\beta mL} \tag{6.17}$$

If we assume gain is proportional to current, we see that the fringe shape and contrast improves

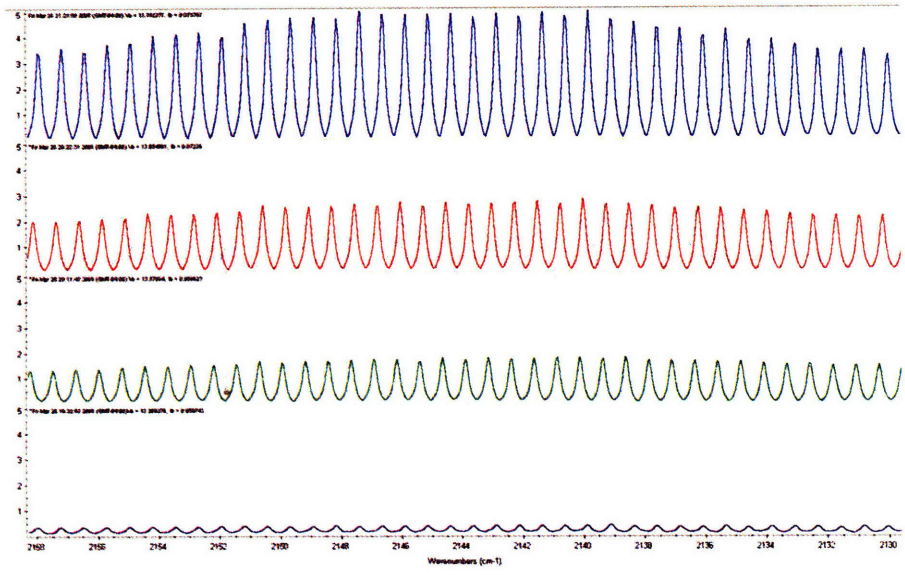

Figure 6-5: Amplified Spontaneous Emission Spectra for various biases - bias is increasing from bottom to top

as losses are reduced. Furthermore, we can take the fourier transform of 6.17 which forms a

delta function comb.

$$FT[I(\beta)] = \frac{(1-R)^2}{R}\left[\cdots FT\left[\frac{b[\beta]}{1-b[\beta]^2}(b[\beta])^m e^{4\pi n\beta mL}\right] + FT\left[\frac{b[\beta]}{1-b[\beta]^2}(b[\beta])^{m+1} e^{4\pi n\beta(m+1)L}\right]\cdots\right] \tag{6.18}$$

(6.19)

We can simplify the expression using knowledge about fourier transforms where we define the fourier transform of variables of $\beta \rightarrow \gamma$

$$FT\left[\frac{b[\beta]}{1-b[\beta]^2}(b[\beta])^m\right] * \delta(\gamma - 4\pi n(m)L) \tag{6.20}$$

$$W_m(\gamma) = FT\left[\frac{b[\beta]}{1-b[\beta]^2}(b[\beta])^m\right] \tag{6.21}$$

This is significant since we derived the situation assuming we have the transmission spectra

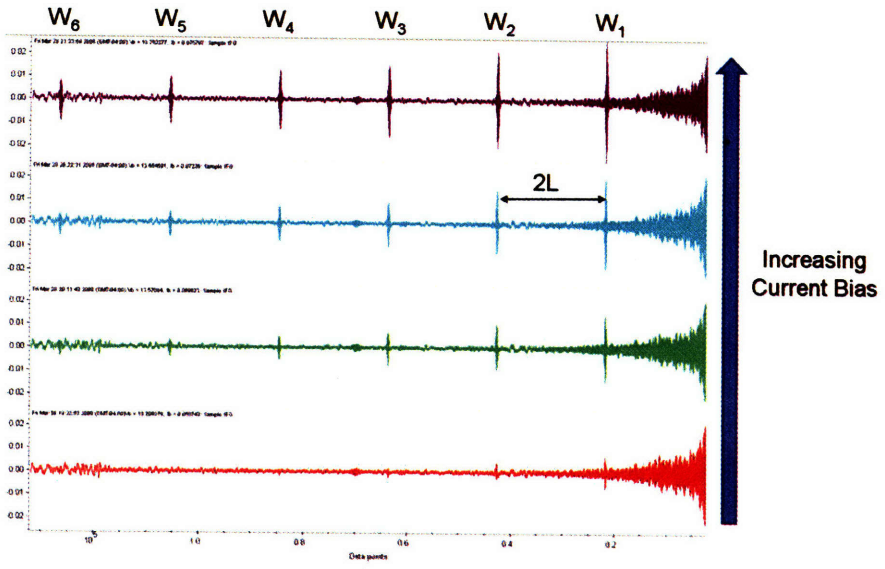

Figure 6-6: Fourier Transform of ASE - Interferogram of raw data

from a device; however, as is commonly with fourier transform spectroscopy we get the spectra by taking the fourier transform of the interferogram. In figure 6-6 we see the Fourier Transform of the spectra, where it is indeed a periodic delta function train. From a physical perspective, each of the peaks represents light undergoing a round-trip in the cavity, therefore as the bias and gain is increased, we see that the number of round-trips that the light can under go starts to increase, which is evident by the number of distinct peaks from the interferogram.

The periodically spaced delta functions in the Interferogram have also been convolved with the precursor function which we define as $W(\gamma)$. Therefore, if we have the Interferogram and assuming the bandwidth of our gain function is narrow with respect to the spacing of the delta functions, from $W_m(\gamma)$ and $W_{m+1}(\gamma)$, we can solve for $b(\beta)$

$$b[\beta] = \frac{IFT[W_{m+1}(\gamma)]}{IFT[W_m(\gamma)]} = \left[\frac{b[\beta]}{1-b[\beta]^2}(b[\beta])^{m+1}\right] / \left[\frac{b[\beta]}{1-b[\beta]^2}(b[\beta])^{m}\right] \tag{6.22}$$

So experimentally, we can compute the b versus wavenumber. which now we need to correlate back to the loss and gain.

$$b[\beta] = Re^{-[\alpha_{wg}-G(\beta)]L} \tag{6.23}$$

$$b[\beta, I] = Re^{-[\alpha_{wg}-g(\beta)I]L} \tag{6.24}$$

$$\alpha_{wg} - G(\beta) = -\frac{1}{L}\ln\left[\frac{b[\beta, I]}{R}\right] \tag{6.25}$$

$$\alpha_{wg} - g(\beta)I = -\frac{1}{L}\ln\left[\frac{b[\beta, I]}{R}\right] \tag{6.26}$$

Where I is the current. We assume for most of these devices that the gain increases linearly with current, which appears valid for the Mid-IR. Therefore if we assume zero gain at no bias, then all the loss is due to the waveguide. Figure 6-7 shows the resulting left hand side of equation 6.26, which by plotting the gain versus current we can obtain a waveguide loss by computing the y intercept as seen in Figure 6-8 By computing the intercept we computed a waveguide loss of 1.2307 1/cm, which is close to expected losses from simulation. Experiments were also done on 606 device with $3 \times 10^{17} cm_*^3$ doping, which was 2.2 1/cm. This is reasonable since one would expect the waveguide loss to go up slightly with increased doping. The gain per current density was 7.4 cm/kA.

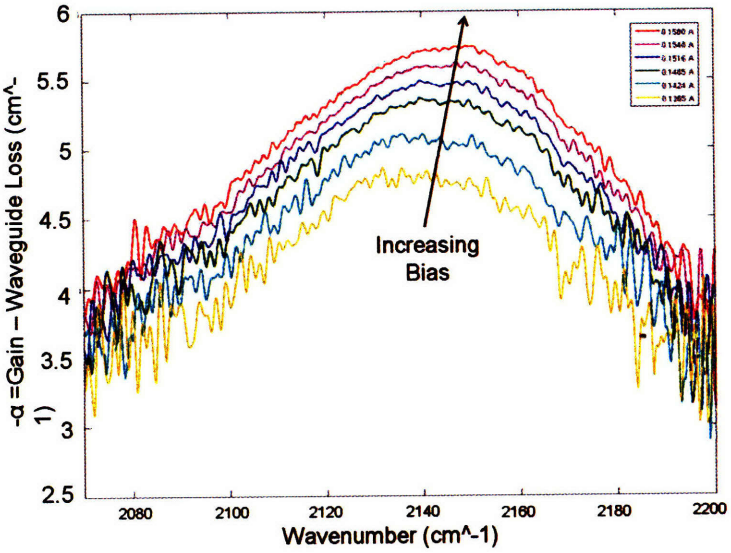

Figure 6-7: Gain versus Bias

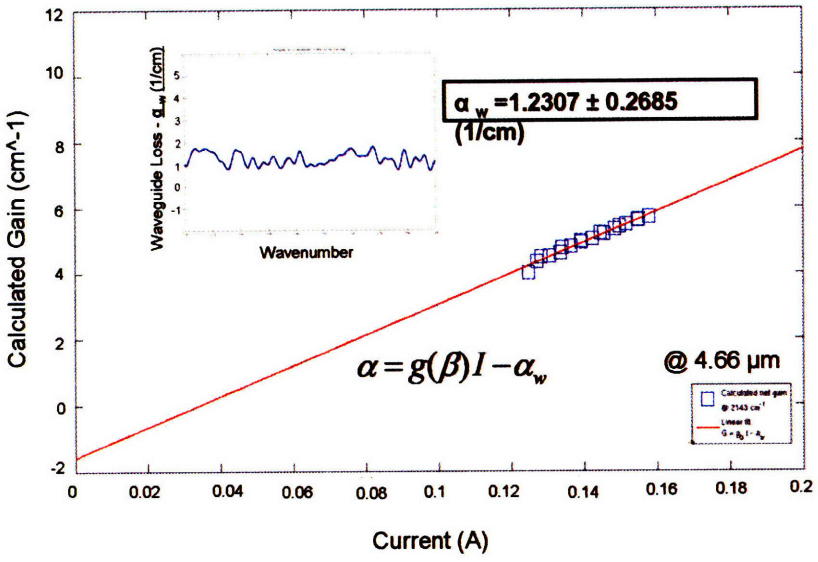

Figure 6-8: Gain Versus Current for 07-605 Sample, 2mm long, 8 μm

There were some initial issues experimentally with this experiment. First, we initially tried to do this in a pulsed mode operation, but were never able to obtain clear fringes. This was mainly due to washed out features from our devices due to transient effects and also reduced power in pulsed mode. Only by running the devices in CW and at 77K, were we able to drive enough power through these devices safely. Furthermore, issues with the Winston cone for collection caused some strange artifacts and collection of higher order modes, which skewed our data collection. Therefore, the devices measured had to be relatively narrow to avoid generating ASE from higher order modes. Furthermore, some higher level data processing was done to filter out noise on the interferegram caused by blackbody and spectral information not relevant to our device operation regime. The filter window used and the results are shown in Figure 6-9 and 6-10, which can be compared to figure 6-6 to see the improvement of the inteferrogram after data processing.

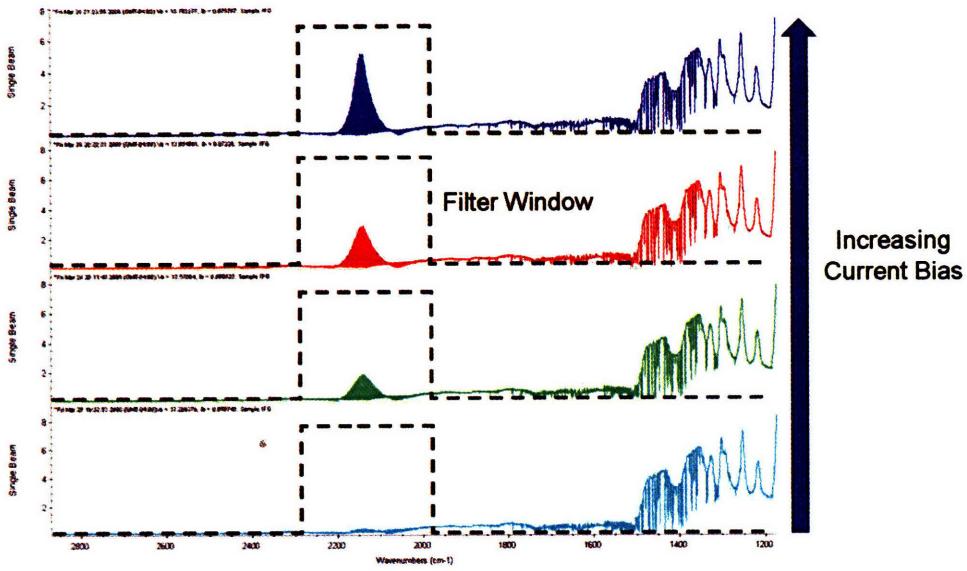

Figure 6-9: Filter Window for reprocessing the Interferogram

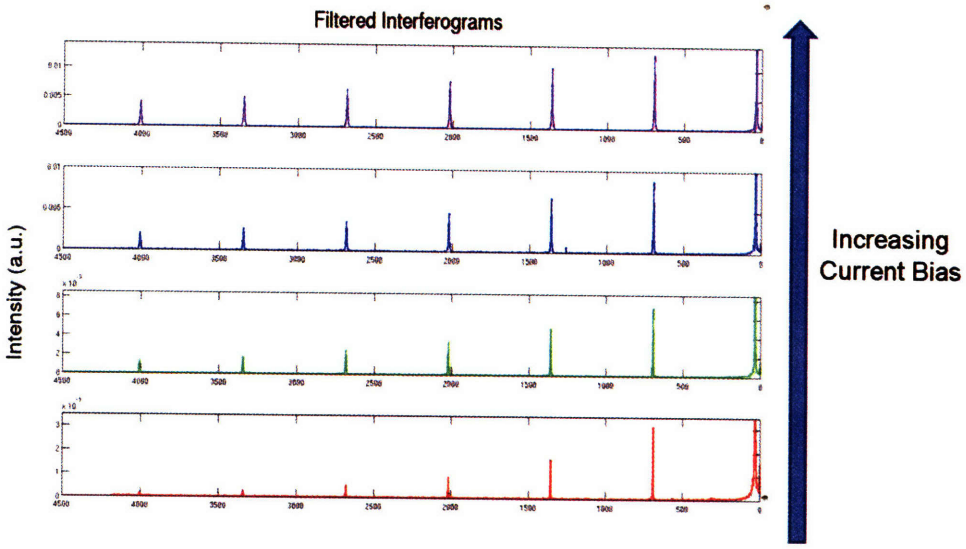

Figure 6-10: Results from Filtered Interferogram

6.2 MIT-LL Injectorless 1

The MIT Injectorless 1 structure was grown and fabricated into laser ridges for the purposes of measuring EL or spectrum emission. Unfortunately, there seems to be a lot of device to device variation in the fabrication. The device was initially wet-etched, but the bonding pads did not make good contact with the ridge of the device. Therefore, the device was re-fabricated using ICP-dry etched ridges, which showed some nominal conduction. Unfortunately, even amongst this batch of devices there was device to device variation. Figures 6-11 and 6-12 show the differences between different bars from the same wafer. It is believed the later which shows much larger current is mainly due to a fabrication induced parasitic current channel. Most devices appear to drive very little current. The current density in figure 6-11 is an order of magnitude smaller than for normal QCL device operation. For both devices, some type of emission was observed; however, the emission wavelength occurs at 1.562 μm, which corresponds roughly to the band gap of the InGaAs. Upon further discussion with our collaborators at Lincoln Labs, it appears that due to the high fields across these structure, the InGaAs waveguide layers are perhaps reversed biased avalanche emitted. The spectrum in figure 6-13 holds true for all the bars tested at low temperature.

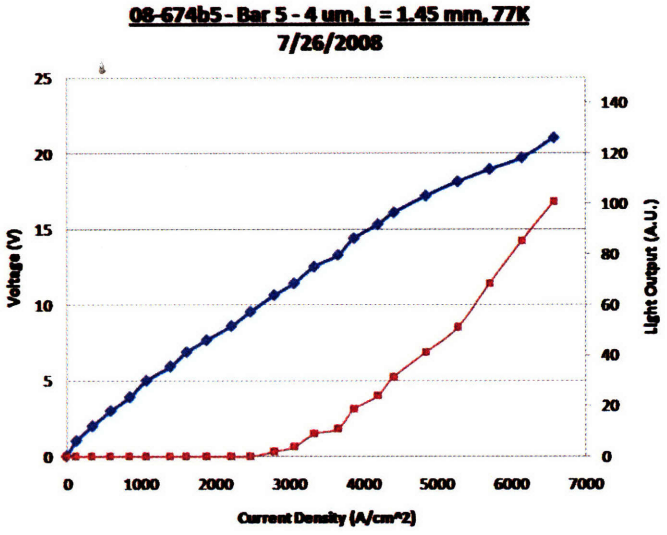

Figure 6-11: LIV from 08-674b5 Bar 5 at 77K. Blue represents IV, Red represents LI

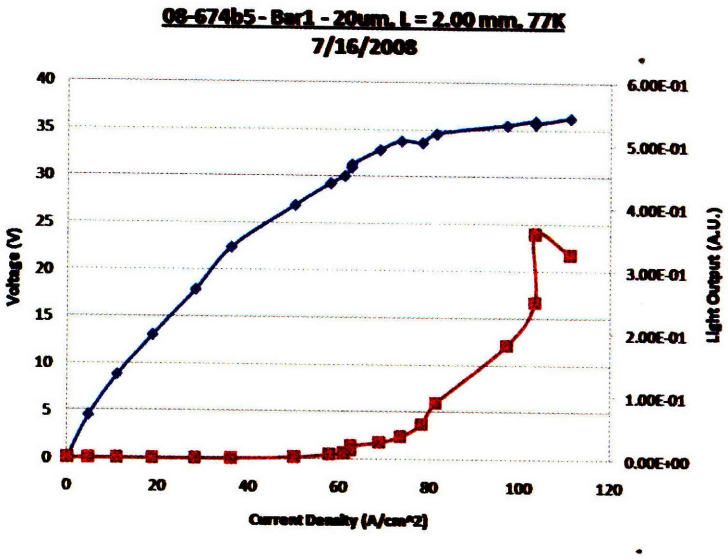

Figure 6-12: LIV from 08-674b5 Bar 1 at 77K. Blue represents IV, Red represents LI

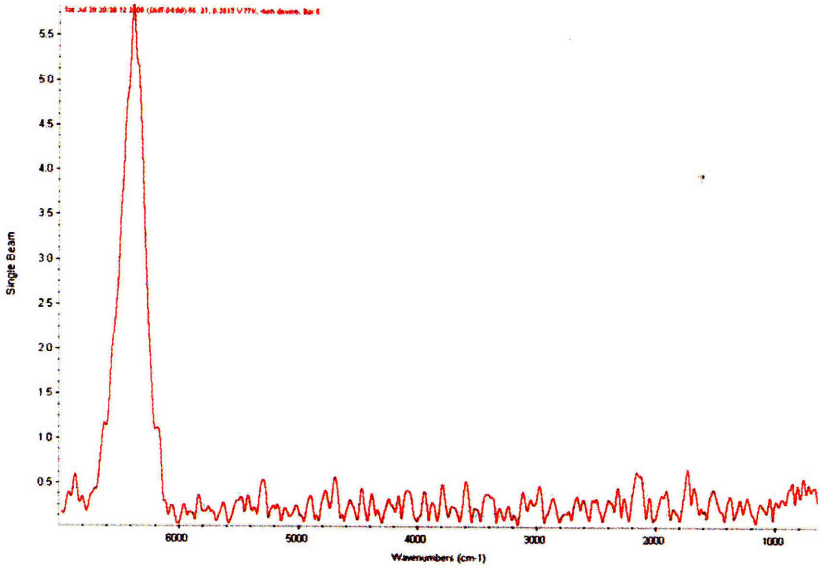

Figure 6-13: Spectrum from 08-674b5 Bar 5 at 77K

6.3 MIT-LL Injectorless 2

After the initial attempt at growing MIT-LL Injectorless 1, MIT-LL Injectorless 2 was grown. Due to the low conductivity from MIT-LL Injectorless 1, two samples were grown: 08-696c5 with $4\times10^{17}cm^{-3}$ doping and 08-697c5 with $2\times10^{17}cm^{-3}$. Furthermore, the samples were abbreviated test structures just to verify the IV. Instead of 45 modules, only a 20 module structure was grown with InGaAs waveguide layers but only a thin InP cladding layer. This was done to conserve resources and time to verify reasonable conduction through these devices. Upon discussions and communications with Christine Wang, the structure's Aluminum and Gallium compositions were apparently off by 2-3 % and the total QCL period length is 4 % longer than designed. This was due to structures grown without xray feedback. Therefore, the IV curves measured at 300K and 77K, in terms of turn on voltages may be slightly off from designed values for this abbreviated structures. Measurements were done at 77K primarily to see if any features due to changes in conductivity from resonant tunneling could be observed. Unfortunately, the IV curves are relatively smooth. The turn on voltages are a little off since the designed peak bias should correspond to 6.8380 V. This hopefully can be attributed to the variations in the growth material parameters. Unfortunately, as of yet, we have no solid explanation about the change in IV between doping. Normally, the IV should scale proportionally with doping; however, that is not the case in figures 6-14 and 6-15. One possibility is a fabrication error for the device causing leakage. It is also possible that oxygen traps caused by the high barrier strain might cause some nonlinear effects with respect to the amount of doping. Unfortunately, until a full laser structure is grown with InP cladding, it will not be known whether or not this structure and material system works.

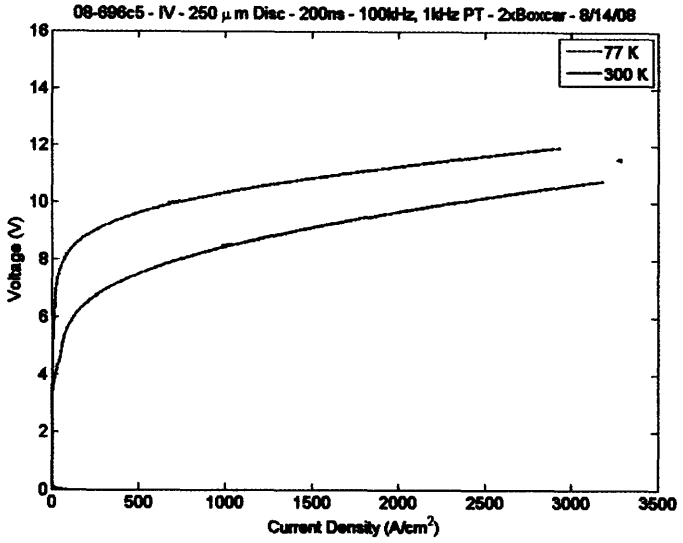

Figure 6-14: IV for 08-696c5 - 77K and 300K, 250 μm disc structures, $4 \times 10^{17} cm^{-3} Doping$

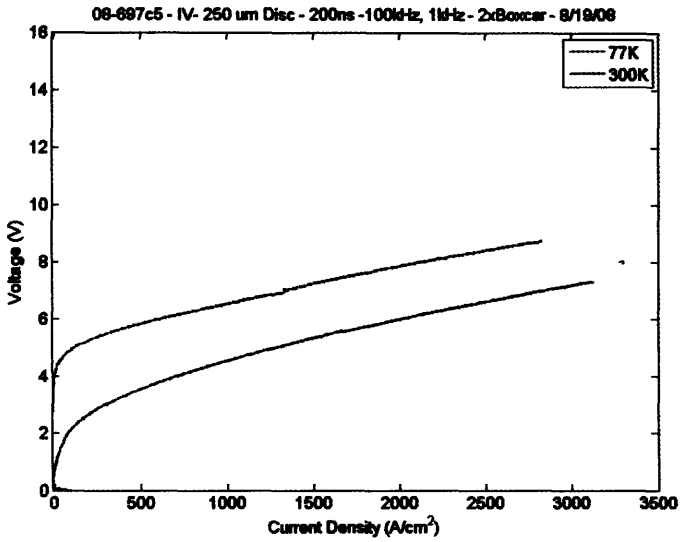

Figure 6-15: IV for 08-697c5 - 77K and 300K, 250 μm disc structures, $2 \times 10^{17} cm^{-3} Doping$

Chapter 7

Conclusion

In this thesis, we have covered all the theory behind Mid-IR QCL lasers. Furthermore, we have explored Monte Carlo simulations for the purpose of simulating Mid-IR QCL devices through inclusion of nonparabolicity. These simulations provided some insights into the internal workings of the QCL and provided some rough agreement with experimentally measured IV's.

Furthermore, we designed an injectorless structure for purposes of obtaining higher wall plug efficiency due to reduced voltage defect. This utilized a new simplified 4 well structure and a novel highly strained material system that has not been explored before. We have also done experimental work on building an experimental setup for testing and measuring these devices. This includes a custom Vacuum chamber, Thermoelectric Controlled temperature stage, and all GPIB software for measurement automation. Furthermore, we demonstrated experimental techniques of measuring waveguide loss through Fourier Transformed Hakki-Paoli measurements. All of which has been crucial for extracting various parameters about device performance.

Finally, we measured some basic test structure for our designs and are currently waiting on full laser structures to be grown and tested. The IV curves for the current batch of devices appears promising in that the devices have reasonable turn on voltages and conduction.

As for future work, continuing work is being done on both the simulation, experimental, and design side. As for simulation, further work is being done on exploring a hybrid density matrix and monte carlo simulation to model resonant tunneling across the injection barrier in a QCL structure. This will hopefully provide less noisy IV curves and provide a phenomenological parameter for controlling conduction from module to module. Modifications have already been made to the simulations to included a phenomenological stimulated emission parameter that

couples two states with a fixed scattering rate. This hopefully will allow us to estimate the amount of power and photon density required to cause a specific population inversion. Thus this can manually enforce known conditions of gain clamping into our simulations. As for experimental work, further measurement strategies are being explored to provide further insight into the internal workings of the QCL. Transmission experiments through an active waveguide using a broad band IR source should hopefully allow us to probe the electron subband populations and gain of the device at various bias points. This coupled with our monte carlo simulations should prove quite interesting for our injectorless structures. Due to the simplicity of the 4 well structure, we would expect interpretation and data to be much cleaner due to the reduced number of bound states. As for designs and materials, Christine Wang is currently undergoing modifications to MOCVD reactor to provide better flow control of her Gallium and Aluminum sources for growing sharper interfaces at these high strains and consequently high growth rates. We are also exploring 5 well structures for future designs in order to further reduce parasitic channels as well as lower strained composition structures for debugging purposes if these high strained structures continue to provide unusual device characteristics.

Overall, in terms of wall plug efficiency, the injectorless design is an unexplored option for achieving better performance. Hopefully, through a more systematic study with our collaborators at Lincoln Labs we can achieve higher wall plug efficiency.

Bibliography

[1] K. Faist, D. Hofstetter, M. Beck, T. Aellen, M. Rochat, and S. Blaser. Bound-to-continuum and two-phonon resonance, quantum-cascade lasers for high duty cycle, high-temperature operation. *Quantum Electronics, IEEE Journal of*, 38(6):533–546, Jun 2002.

[2] A. Friedrich, C. Huber, G. Boehm, and M.-C. Amann. Low-threshold room-temperature operation of injectorless quantum-cascade lasers: influence of doping density. *Electronics Letters*, 42(21):1228–1229, Oct. 2006.

[3] A. Evans, S. R. Darvish, S. Slivken, J. Nguyen, Y. Bai, and M. Razeghi. Buried heterostructure quantum cascade lasers with high continuous-wave wall plug efficiency. *Applied Physics Letters*, 91(7):071101, 2007.

[4] Jerome Faist, Federico Capasso, Deborah L. Sivco, Carlo Sirtori, Albert L. Hutchinson, and Alfred Y. Cho. Quantum Cascade Laser. *Science*, 264(5158):553–556, 1994.

[5] A. Lyakh, C. Pflügl, L. Diehl, Q. J. Wang, Federico Capasso, X. J. Wang, J. Y. Fan, T. Tanbun-Ek, R. Maulini, A. Tsekoun, R. Go, and C. Kumar N. Patel. 1.6 w high wall plug efficiency, continuous-wave room temperature quantum cascade laser emitting at 4.6 mu m. *Applied Physics Letters*, 92(11):111110, 2008.

[6] R.F. Kazarinov and R.A. Suris. Possibility of the amplification of electromagnetic waves in a semiconductor with a superlattice. *Sov. Phys. Semi.*, 5(4), 1971.

[7] Andrea Friedrich, Gerhard Boehm, Markus Christian Amann, and Giuseppe Scarpa. Quantum-cascade lasers without injector regions operating above room temperature. *Applied Physics Letters*, 86(16):161114, 2005.

[8] A Friedrich, G Boehm, and M C Amann. Short-wavelength intersubband staircase lasers, with and without alas-blocking barriers. *Semiconductor Science and Technology*, 22(3):218–221, 2007.

[9] Gerald Bastard. *Wave Mechanics Applied to Semiconductor Heterostructures.* Monographies de physique. Les Editions de Physique, Les Ulis Cedex, France, 1988.

[10] Shun Lien Chuang. *Physics of Optoelectronic Devices.* Wiley series in pure and applied optics. Wiley, New York, 1995.

[11] Carlo Sirtori, Federico Capasso, Jérôme Faist, and Sandro Scandolo. Nonparabolicity and a sum rule associated with bound-to-bound and bound-to-continuum intersubband transitions in quantum wells. *Phys. Rev. B*, 50(12):8663–8674, Sep 1994.

[12] Amnon Yariv. *Quantum Electronics.* Wiley, New York, 3rd ed edition, 1989.

[13] Anthony E. Siegman. *Lasers.* University Science Books, Mill Valley, California, 1986.

[14] Benjamin S Williams and Massachusetts Institute of Technology. *Terahertz Quantum Cascade Lasers.* 2003.

[15] Roberto Paiella. *Intersubband Transitions in Quantum Structures.* McGraw-Hill nanoscience and technology series. McGraw-Hill, New York, 2006.

[16] Hans Callebaut and Massachusetts Institute of Technology. *Analysis of the Electron Transport Properties in Quantum Cascade Lasers.* 2006.

[17] Mark Lundstrom. *Fundamentals of Carrier Transport.* Cambridge University Press, New York, 2000.

[18] C. Sirtori, F. Capasso, J. Faist, A.L. Hutchinson, D.L. Sivco, and A.Y. Cho. Resonant tunneling in quantum cascade lasers. *Quantum Electronics, IEEE Journal of*, 34(9):1722–1729, Sep 1998.

[19] H. C Liu and Federico Capasso. *Intersubband Transitions in Quantum Wells: Physics and Device Applications.* Semiconductors and semimetals. Academic Press, San Diego, CA, 2000.

[20] Jérôme Faist. Wallplug efficiency of quantum cascade lasers: Critical parameters and fundamental limits. *Applied Physics Letters*, 90(25):253512, 2007.

[21] Rita C. Iotti and Fausto Rossi. Microscopic theory of hot-carrier relaxation in semiconductor-based quantum-cascade lasers. *Applied Physics Letters*, 76(16):2265–2267, 2000.

[22] P. Harrison. *Quantum Wells, Wires, and Dots: Theoretical and Computational Physics.* Wiley, Chichester, 2000.

[23] I. Vurgaftman, J. R. Meyer, and L. R. Ram-Mohan. Band parameters for iii–v compound semiconductors and their alloys. *Journal of Applied Physics*, 89(11):5815–5875, 2001.

[24] Andrea Friedrich, Gerhard Boehm, Markus Christian Amann, and Giuseppe Scarpa. Quantum-cascade lasers without injector regions operating above room temperature. *Applied Physics Letters*, 86(16):161114, 2005.

[25] Daniel Hofstetter, Mattias Beck, Thierry Aellen, and Jérôme Faist. High-temperature operation of distributed feedback quantum-cascade lasers at 5.3 mu m. *Applied Physics Letters*, 78(4):396–398, 2001.

[26] A. Evans, J. Nguyen, S. Slivken, J. S. Yu, S. R. Darvish, and M. Razeghi. Quantum-cascade lasers operating in continuous-wave mode above 90 [degree]c at lambda 5.25 mu m. *Applied Physics Letters*, 88(5):051105, 2006.

[27] A. Evans, J. S. Yu, S. Slivken, and M. Razeghi. Continuous-wave operation of lambda 4.8 mu m quantum-cascade lasers at room temperature. *Applied Physics Letters*, 85(12):2166–2168, 2004.

[28] A Friedrich, G Boehm, and M C Amann. Short-wavelength intersubband staircase lasers, with and without alas-blocking barriers. *Semiconductor Science and Technology*, 22(3):218–221, 2007.

[29] Chris G. Van de Walle. Band lineups and deformation potentials in the model-solid theory. *Phys. Rev. B*, 39(3):1871–1883, Jan 1989.

[30] N.J. Ekins-Daukes, K. Kawaguchi, and J. Zhang. Strain-balanced criteria for multiple quantum well structures and its signature in x-ray rocking curves. *Crystal Growth and Design*, 2(4):287–292, 2002.

[31] T. Gresch, M. Giovannini, N. Hoyer, and J. Faist. Quantum cascade lasers with large optical waveguides. *Photonics Technology Letters, IEEE*, 18(3):544–546, 1, 2006.

[32] Basil W. Hakki and Thomas L. Paoli. cw degradation at 300[degree]k of gaas double-heterostructure junction lasers. ii. electronic gain. *Journal of Applied Physics*, 44(9):4113–4119, 1973.

[33] Basil W. Hakki and Thomas L. Paoli. Gain spectra in gaas double - heterostructure injection lasers. *Journal of Applied Physics*, 46(3):1299–1306, 1975.

[34] Daniel Hofstetter and Robert L. Thornton. Theory of loss measurements of fabry perot resonators by fourier analysis of the transmission spectra. *Opt. Lett.*, 22(24):1831–1833, 1997.

[35] Daniel Hofstetter and Robert L. Thornton. Loss measurements on semiconductor lasers by fourier analysis of the emission spectra. *Applied Physics Letters*, 72(4):404–406, 1998.

[36] D. Hofstetter and J. Faist. Measurement of semiconductor laser gain and dispersion curves utilizing fourier transforms of the emission spectra. *Photonics Technology Letters, IEEE*, 11(11):1372–1374, Nov 1999.